NASA-CR-197746

MCAT Institute
Final Report
95-02

(NASA-CR-197746) PROGRESS IN INCOMPRESSIBLE NAVIER-STOKES COMPUTATIONS FOR PROPULSION FLOWS AND ITS DUAL-USE APPLICATIONS Final Report (MCAT Inst.) 37 p

N95-26766

Unclas

G3/34 0048505

Progress in Incompressible Navier–Stokes Computations for Propulsion Flows and Its Dual–Use Applications

Cetin Kiris

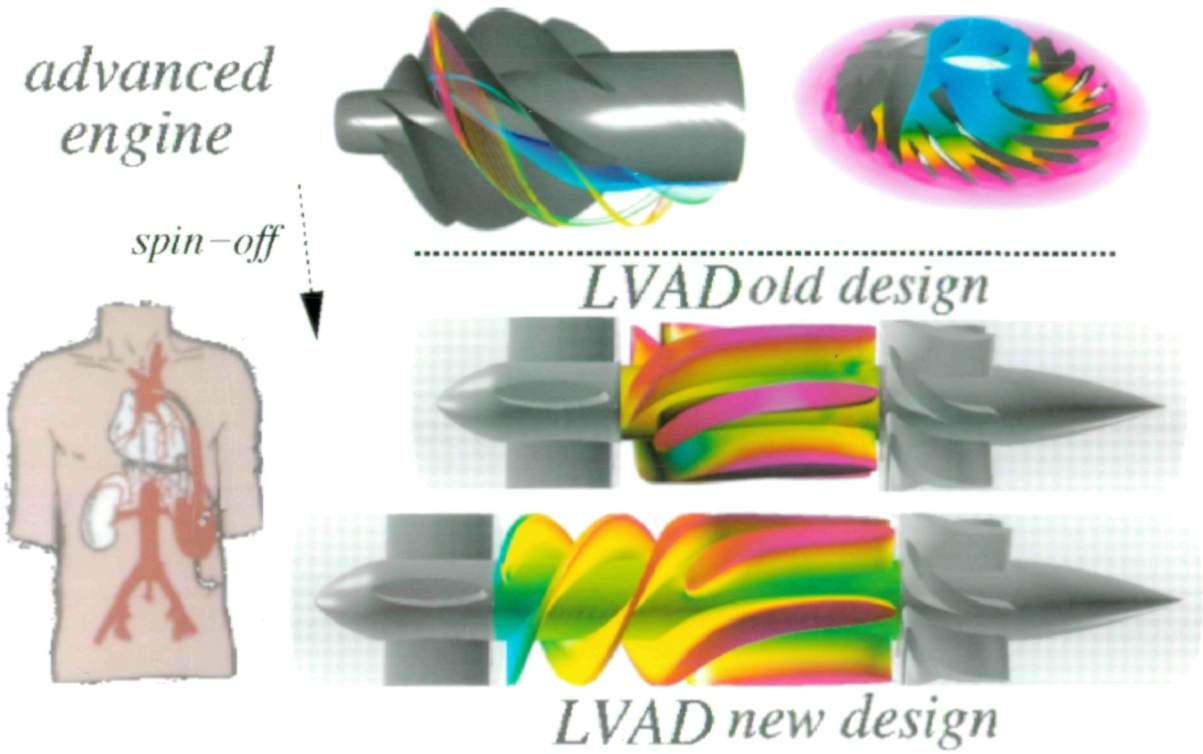

January, 1995

NCC2–500

MCAT Institute
3933 Blue Gum Drive
San Jose, CA 95127

PROGRESS IN INCOMPRESSIBLE NAVIER-STOKES COMPUTATIONS FOR PROPULSION FLOWS AND ITS DUAL-USE APPLICATIONS

Cetin Kiris
MCAT Institute
NASA Ames Research Center
Mail Stop T27B-1
Moffett Field, CA 94035

ORIGINAL CONTAINS
COLOR ILLUSTRATIONS

Abstract

Development of an incompressible Navier-Stokes solution procedure was performed for the analysis of a liquid rocket engine pump components and for the mechanical heart assist devices. The solution procedure for the propulsion systems is applicable to incompressible Navier-Stokes flows in a steadily rotating frame of reference for any general complex configurations. The computer codes were tested on different complex configurations such as liquid rocket engine inducer and impellers. As a spin-off technology from the turbopump component simulations, the flow analysis for an axial heart pump was conducted. The baseline Left Ventricular Assist Device (LVAD) design was improved by adding an inducer geometry by adapting from the liquid rocket engine pump. The time-accurate mode of the incompressible Navier-Stokes code was validated with flapping foil experiment by using different domain decomposition methods. In the flapping foil experiment, two upstream NACA 0025 foils perform high-frequency synchronized motion and generate unsteady flow conditions for a downstream larger stationary foil. Fairly good agreement was obtained between unsteady experimental data and numerical results from two different moving boundary procedures. Incompressible Navier-Stokes code (INS3D) has been extended for heat transfer applications. The temperature equation was written for both forced and natural convection phenomena. Flow in a square duct case was used for the validation of the code in both natural and forced convection.

1. Introduction

Computational fluid dynamics has been developed to a level where it has become an indispensable part of aerospace research and design. advanced component systems in the next generation of transport vehicles, such as advanced liquid rocket engine fuel systems, marine propulsion systems, and high-lift configurations, are likely to require more efficient and simpler designs with lower manufacturing costs. Fast and reliable incompressible flow simulation capabilities are crucial to developing these new designs. For example, in order to understand the source of the noise generated by a high-lift wing-flap system, the unsteady flowfield around these configurations must be resolved accurately.

The cover illustration shows the particle traces colored by relative velocity magnitude in the liquid rocket engine inducer, the pressure contours for the Space Shuttle Main Engine HFFTP Impeller, and the pressure contours for the old and new designs of the NASA-JSC/Baylor College of Medicine Left Ventricular Assist Device (LVAD).

Second example of a viscous incompressible flowfield is the rotor-stator interaction in turbomachinery. A flange-to-flange rocket engine fuel-pump simulation must account for the interaction between the rotating and non-rotating components: the flow straighteners, the impeller, the volute and diffusers. Such incompressible flow simulation capability can also be beneficial to other applications, such as the development of artificial heart devices. A Ventricular Assist Device (VAD) developed by NASA Johnson Space Center (JSC) and Baylor College of Medicine (BCOM) has a design similar to a rocket engine fuel pump in that it also consists of a flow straightener, an impeller, and a diffuser.[1] Technology developed for aerospace applications can be utilized for the benefit of human health. Accurate and detailed knowledge of the flowfield obtained by steady and unsteady incompressible flow calculations can be greatly beneficial to designers in their effort to reduce the cost and improve the reliability of these devices.

Analysis of biofluid flow problems are challenging and the potential impact of an advanced computational tool on medical research for improving health care is enormous. For example, the blood flow through mechanical hearts, heart assist devices, and heart valves is unsteady and involves moving walls making experimental study very difficult. Computational analysis offers an alternative to experimental methods which can produce flow field data in great detail. Medical researchers can study this extensive data to obtain a better understanding of the flow physics. Computational analysis can also be used to optimize the design of mechanical devices at a significantly lower cost and time than required by an empirical approach.

In addition to the geometric complexities, a variety of flow phenomena are encountered in biofluids. These include turbulent boundary layer separation, wakes, transition, tip vortex resolution, three-dimensional effects, and Reynolds number effects. In order to increase the role of Computational Fluid Dynamics (CFD) in the design process, the CFD analysis tools must be evaluated and validated so that designers gain confidence in their use. The incompressible flow solver, INS3D, has been applied to various viscous flow problems and extensively validated.[2-13] This report presents a continuation of this validation effort for the turbulent flow in a liquid rocket engine pump components in a steadily rotating frame of reference, for time-accurate calculations with moving boundaries, and for incompressible flows with heat transfer. In the report, it is also presented how computational flow simulation capability developed for liquid rocket engine pump component analysis has been applied to the Left Ventricular Assist Device being developed jointly by NASA JSC and Baylor College of Medicine.

2. Algorithm

The algorithm is based on the pseudocompressibility method as developed by Chorin.[14] The pseudocompressibility algorithm introduces a time-derivative of the pressure term into the continuity equation; the elliptic-parabolic type partial differential equations are transformed into the hyperbolic-parabolic type. The original version of the INS3D code[2-3] with pseudocompressibility approach utilized the Beam-Warming[15] approximate factorization algorithm and central differencing of the convective terms. Since the convective terms of the resulting equations are hyperbolic, upwind differencing can be applied to these terms. The current versions of the INS3D code use flux-difference splitting based on the method

of Roe.[16] Chakravarthy[17] outlines a class of high-accuracy flux-differencing schemes for the compressible flow equations. Following the third-order upwind differencing, a fifth-order-accurate, upwind-biased stencil was derived by Rai.[18] The third- and fifth-order upwind differencing used here is an implementation of these schemes for the incompressible Navier-Stokes equations. The upwind differencing leads to a more diagonal dominant system than does central differencing and does not require a user-specified artificial dissipation. The viscous flux derivatives are computed by using central differencing. In the steady-state formulation, the time derivatives are differenced using the Euler backward formula. The equations are solved iteratively in pseudo-time until the solution converges to a steady state. In the time-accurate formulation, the equations are iterated to convergence in pseudo-time for each physical time step until the divergence of the velocity field has been reduced below a specified tolerance value.

The matrix equation is solved iteratively by using a nonfactored Gauss-Seidel type line-relaxation scheme,[19] which maintains stability and allows a large pseudo-time step to be taken. Details of the numerical method can be found in Refs. 4-5. The present calculations use the one-equation turbulence model developed by Baldwin and Barth.[20] In this model, the transport equation for the turbulent Reynolds number is derived from a simplified form of the standard $k - \epsilon$ model equations. The model is relatively easy to implement because there is no need to define an algebraic length scale. The transport equation is solved by using the same Gauss-Seidel type line-relaxation scheme as the mean-flow equations.

3. Liquid Rocket Engine Pump Components

Until recently, the high performance pump design process was not significantly different from that of three decades ago. During this time, a vast amount of experimental and operational experience has demonstrated that there are many important features of pump flows that are not accounted for in the current semi-empirical design process. Pumps being designed today are no more technologically advanced than those designed for the Space Shuttle Main Engine (SSME). During that same time span, huge strides have been made in computers, numerical algorithms, and physical modeling. One major accomplishment of this work is to extend CFD technology by validating an advanced CFD code for pump flows and demonstrating their value to pump designers.

The validation effort for pump components has focused on inducers and impellers.[9-10] The computed results from a numerical simulation of the flow through a rocket pump inducer were compared with experimental measurements. The design of an advanced impeller was verified by simulating the flow through the baseline and the optimized geometries. The effects of the vaneless space in the advanced impeller concept were investigated by using the incompressible Navier-Stokes flow simulation capability. The comparisons reported in Ref. 9-10 showed that the computations compared well with experiments. The resulting computational procedure with the one-equation Baldwin-Barth turbulence model was applied to the flow through the SSME High Pressure Fuel Turbo-Pump (HPFTP) impeller. The SSME-HPFTP impeller has 6 full blades, 6 long partial blades, and 12 short partial blades. The impeller wheel speed is 6,300 rpm, and the Reynolds number for this calculation is 181,000 per inch. Figure 1 shows the nondimensional pressure contours on the

hub surface of the impeller. Since the pressure rise between the impeller inlet and the exit is quite large, the pressure variations between the suction and the pressure sides of the blades are not noticable from this figure. This calculation includes the vaneless space between the impeller trailing edge and the diffuser vane leading edge. Figure 2 shows blade-to-blade velocity and flow angle distributions at two stations downstream from the SSME-HPFTP impeller exit. Blade-to-blade velocity distribution illustrates the impeller exit flow distortion. Solid lines represent the experimental data and dashed lines represent computed results. The jet-wake pattern, which produces an unsteady load on the diffuser vanes, was captured at both meridional locations. The numerical results compare reasonably well with the experimental data. The pressure contours in Figure 1 also indicates this jet-wake pattern.

4. Left Ventricular Assist Device

In 1989, NASA Johnson Space Center (JSC) began a joint project with the DeBakey Heart Center of the Baylor College of Medicine (BCOM) in Houston to develop a new implantable LVAD prototype system. This LVAD is based on a fast rotating axial pump requiring a minimum number of moving parts. To make it implantable, the device has been made as small as possible, requiring a very high rotational speed. The computational procedure described above for pump components has been used to provide the designers with a view of the complicated fluid dynamic processes inside this device. Due to the nature of the device, this detailed information cannot be obtained experimentally. The detailed computational look at the fluid flow is very important to the designers; high levels of turbulence can damage the red blood cells and regions of recirculating flow can lead to blood clots. Thus the ability to predict these phenomena can greatly help the designers.

The flow through the baseline design of the LVAD impeller was numerically simulated by solving the incompressible Navier-Stokes equations in a steady rotating frame of reference. Zonal multiblock grids were used in this component analysis. The geometry and the computational grid of the LVAD baseline impeller are shown in Figure 3. The domain is divided into five zones with dimensions of 127 x 39 x 33, 127 x 39 x 33, 59 x 21 x 7, 47 x 21 x 5, and 59 x 21 x 7, respectively. Zone 1 is the region between the suction side of the partial blade and the pressure side of the full blade; the region between the pressure side of the partial blade and the suction side of the full blade is filled by zone 2; and zones 3 through 5 allow tip-leakage effects to be included in the computational study and occupy the regions between the impeller blade tip and the casing. At the zonal interfaces, grid points were matched one-to-one. For all zones, an H-H type grid topology was used. An H-type surface grid was generated for each surface using an elliptic grid generator. The interior region of the three-dimensional grid was filled using an algebraic grid generator coupled with an elliptic smoother. Periodic boundary conditions were used at the end points in the rotational direction. The design flow of this impeller is 5 liters per minute and the design speed is 12,600 revolutions per minute (rpm). The problem was nondimensionalized by the tube diameter (0.488 inches) and the impeller tip velocity. The solution was considered converged when the maximum residual had dropped at least five orders of magnitude. Computer time required per grid point per iteration was about 1.5×10^{-4} seconds. The total computer time required for these calculations was about 6 to 8 single

processor Cray-C90 hours. A parametric study was performed to optimize the impeller blade shape and the tip clearance. Initially, three different impeller blade designs with a tip clearance of 0.009 inches were analyzed. Figure 4 shows the axial velocity contours at the exit plane of the impeller for various blade curvatures. Design III shows massive seperation near the suction side of the partial blade trailing edge because of the high curvature blade shape. Design II, which has less blade curvature than design I, shows flow features very similar to design I. Design I was analyzed with two tip clearances; the tip clearance of 0.0045 inches shows better hydrodynamic performance in terms of efficiency and head coefficient than with a tip clearance of 0.009 inches. Using the design I with a tip clearance of 0.0045 inches as the baseline impeller design, ideas from rocket propulsion and medical science were combined to develop a new implantable LVAD. In collaboration with the NASA-JSC engineering team and BCOM researchers, a new design consisting of the baseline impeller plus an inducer was investigated. The hub and blade surfaces of the baseline impeller and the new impeller are colored by nondimensionalized pressure in Figure 5. The pressure is nondimensionalized by ρV^2, where ρ is the density and V is the impeller tip velocity. The pressure gradient across the blades due to the action of centrifugal force, and the pressure rise from inflow to outflow are shown. The table in Figure 5 shows the clinical results obtained by BCOM. Further clinical hemolysis testing and animal implantation by BCOM are currently underway using the new inducer-impeller design. The hemolysis index reported in Figure 5 shows the amount of hemoglobin generated by the pump in grams per 100 liters. Hemoglobin release can be due to regions of high shear and separated flows. The new design shows a remarkable improvement in performance over the baseline design. The inducer provides a sufficient pressure rise to the flow in order to prevent the cavitation on the impeller blades. Figure 6 shows the particle traces through the new impeller. The traces are colored by the relative total-velocity magnitude. The particles were released near the inducer leading edge, the hub, the inducer blade pressure side, and the tip regions. The swirling motion of the particles indicates a secondary flow region between the partial and the full blades. The particles released near the pressure side of the blade indicate a radial velocity component inside the blade boundary layer. The particles tend to flow from the hub to the tip of the blade. The particles near the inducer leading edge and full blade trailing edge indicate the presence of a back flow.

In the next step of the design process, this computational analysis tool will be used to improve the diffuser geometry and the bearing design. This unique insight into the internal fluid structures will lead to improved components for an improved heart assist device. In July 1991, the Institute of Medicine estimated that approximately 25,000 to 60,000 patients per year in North America could benefit from an efficient left ventricular assist device. Thus improved designs made possible because of the current work could have a far reaching impact on human health.

5. Heat Transfer

Heat transfer in viscous incompressible flow is of great interest in many engineering applications. For example, in a liquid rocket engine, the liquid fuel and oxidizer are used as coolant in various components, and in the LVAD, the electric motor releases heat to the blood flow. In order to predict the effect of the heat transfer, a simplified energy equation

is added to current incompressible Navier-Stokes formulation. The fluid is assumed to be incompressible with constant physical properties except the bouyancy effect due to density variations. Using the Boussinesq approximation for bouyancy force, the incompressible Navier-Stokes equations with temperature equation in nondimensional form can be stated in the following way:

$$\begin{aligned} &\frac{\partial u_i}{\partial x_i} = 0 \\ &\frac{\partial u_i}{\partial t} + \frac{\partial u_i u_j}{\partial x_j} = -\frac{\partial p}{\partial x_i} + C_v \nabla^2 u - \vec{e}_g C_b T \\ &\frac{\partial T}{\partial t} + \frac{\partial T u_j}{\partial x_j} = C_t \nabla^2 T \end{aligned} \tag{1}$$

where u_i is the corresponding velocity components, p the pressure, T the temperature, t the time, and x_i the cartesian coordinates. C_v, C_b, and C_t are nondimensional coefficients which are defined as for forced (or mixed) convection,

$$C_v = \frac{1}{Re}, \quad C_b = \frac{Gr}{Re^2}, \quad C_t = \frac{1}{RePr}$$

and for natural convection,

$$C_v = Pr, \quad C_b = RaPr, \quad C_t = 1$$

where

$$Re = \frac{u_o l_o}{\nu}, \quad Pr = \frac{\nu}{\alpha}$$

$$Gr = \frac{g\bar{\beta} l_o^3 (T_1 - T_o)}{\nu^2}, \quad Ra = \frac{g\bar{\beta} l_o^3 (T_1 - T_o)}{\nu\alpha}$$

Here, u_o, is the reference velocity, l_o the reference lenght, $(T_1 - T_0)$, is the reference temperature difference, ν the kinematic viscosity, α the thermal diffusivity, and $\bar{\beta}$ the coeficient of expansion. For natural convection, the reference velocity u_o is replaced by α/l_o in the nondimensionalization procedure.

In order to validate the current heat-transfer formulation with Boussinesq approximation, fluid flow with heat transfer in a square cavity is considered. First, forced convection problem was solved by setting $Gr = 0$. In this case the momentum equations and the temperature equation are decoupled. A 83 x 83 mesh was used for the Reynolds number 400. The computed velocity magnitde and temperature contours for this driven-cavity flow is ploted in Figure 7. Figure 7 also shows the boundary conditions used for this computation. A large temperature gradient is observed near the hot and cold vertical walls. Forced convection results show very good agreement with previous study reported in reference 21. For the Rayleigh number 10,000, free convection results are presented in Figure 8. In this case, the lid remains stationary, and an oposite direction vortex to the one in the forced convection case is formed due to heat transfer. The temperature distribution shows very good agreement with computed results obtained by velocity-vorticity formulation.[21] Figure

9 plots u velocity component along the vertical midplane and v velocity component along the horizontal midplane. Along the midplanes, the peak values of the velocity components reported in reference 21 were also plotted. Very good agreement is obtained between the two. More validation cases for heat transfer will be reported in future.

6. Time-Accurate Calculations

The validation effort for pump flows was extended to unsteady interaction problems by simulating the flapping foil experiment performed by Massachusetts Institute of Technology (MIT). The purpose of the MIT flapping foil experiment (FFX) is to provide detailed unsteady measurements for CFD code validations for the marine propulsion systems. The FFX was designed as a two-dimensional representation of the interaction between the propeller-blade and wake flows. The stationary foil represents a propeller blade embedded in a wake flow generated by upstream pitching foils. The flappers in the FFX generate periodic wake fluctuations which impose an unsteady condition on the stationary foil.

First, steady-state calculations were carried out for overlapped and patched grids in which effects of the grid density and of the order of differencing were investigated. Numerical results showed good agreement with the experimental data. Then, the resulting third-order upwind differencing and Baldwin-Barth one equation turbulence model were applied to unsteady flapping foil calculations. Fairly good agreement was obtained between unsteady experimental data and numerical results from two different moving boundary procedures. Appendix B includes the results from these computations.

7. Conclusions

An efficient and robust solution procedure for 3-D pump component analyses and its spin-off application to an LVAD impeller analysis has been presented. The technique solves the viscous incompressible Navier-Stokes equations with source terms in a steadily rotating reference frame. The method of pseudocompressibility with higher-order accurate upwind differencing and a Gauss-Seidel line relaxation scheme are utilized. The flow through SSME-HPFTP impeller has been successfully simulated. Numerical results which utilize the one-equation Baldwin-Barth turbulence model compare fairly well with experimental data. This validated solution procedure has been applied to the NASA JSC/BCOM LVAD impeller as a design analysis tool. Parametric studies were performed to analyze the performance of the LVAD impeller. Substantial improvements were observed when inducer blades were included upstream of the impeller main blades.

Steady and time-accurate calculations were performed for the MIT flapping foil experiment. A detailed study for the steady-state calculations was performed to investigate the effects of grid topology, grid resolution, and the order of accuracy. A nearly grid independent solution was obtained for the steady FFX simulation by using third-order flux-difference splitting for the convective terms. Unsteady computations were performed using two different grid topologies. Good agreement with experimental mean pressure coefficient were obtained for both grid topologies.

The temperature equation is coupled with momentum equations in order to include heat transfer effect in incompressible flow calculations. Using the Boussinesq approximation for bouyancy force, driven cavity problem was studied for forced and mixed convection case. Very good agreement is obtained between the computed results and the results reported in reference 21.

Acknowledgments

This work was supported by NASA Ames Research Center through Cooperative Agreement NCC 2-500. Computer time was provided by the Numerical Aerodynamic Simulation (NAS) Facility and the Central Computing Facility at NASA Ames Research Center. The author would like to thank NASA JSC and Baylor College of Medicine LVAD Team for providing the LVAD geometry, and the clinical results.

References

1. Aber, G. S., Akkerman, J.W., Bozeman, R. J., and Saucier, D. R., "Development of the NASA / Baylor VAD," NASA Technology 2003 Conference, 1993.

2. Kwak, D., Chang, J. L C., Shanks, S. P., and Chakravarthy, S., "A Three-Dimensional Incompressible Navier-Stokes Flow Solver Using Primitive Variables," *AIAA Journal* , Vol. 24, No. 3, pp. 390-396, 1977.

3. Chang, J., Kwak, D., Rogers, S. E., and Yang, R.-J., "Numerical Simulation Methods of Incompressible Flows and an Application to the Space Shuttle Main Engine," *International Journal of Numerical Methods in Fluids*, Vol 8, pp. 1241-1268, 1988.

4. Rogers, S. E., Kwak, D., "Upwind Differencing for the Time-Accurate Incompressible Navier-Stokes Equations," *AIAA Journal* , Vol. 28, No. 2, pp. 253-262, 1990.

5. Rogers, S. E., Kwak, D. and Kiris, C., "Numerical Solution of the Incompressible Navier-Stokes Equations for Steady and Time-Dependent Problems," *AIAA Journal* , Vol. 29, No. 4, pp. 603-610, 1991.

6. Rogers, S. E., Wiltberger, N. L., and Kwak, D. "Efficient Simulation of Incompressible Viscous Flow Over Single and Multi-Element Airfoils," AIAA Paper No. 92-0405, 1992.

7. Rogers, S. E., "Progress In High-Lift Aerodynamic Calculations," AIAA Paper No. 93-0194, 1993.

8. Rogers, S. E., "A Comparison of Turbulence Models In Computing Multi-Element Airfoil Flows," AIAA Paper No. 94-0291, 1994.

9. Kiris, C., Chang, L., Kwak, D., and Rogers, S. E., "Incompressible Navier-Stokes Computations of Rotating Flows," AIAA Paper No. 93-0678, 1993.

10. Kiris, C. and Kwak, D., "Progress in Incompressible Navier-Stokes Computations for the Analysis of Propulsion Flows," NASA CP 3282, Vol II, Advanced Earth-to-Orbit Propulsion Technology, 1994.

11. Kiris, C. Rogers, S., Kwak, D., and Lee, Y. T., "Time-Accurate Incompressible Navier-Stokes Computations with Overlapped Moving Grids," ASME Fluids Engineering Summer Meeting, Lake Tahoe, Nevada, June 19-23, 1994.

12. Kiris, C., Rogers, S. E., Kwak, D. and Chang, I. "Computation of Incompressible Viscous Flows through Artificial Heart Devices with Moving Boundaries," Fluid Dynamics in Biology, Proceedings of an AMS-IMS-SIAM Joint Research Conference, edited by A.

Y. Cheer and C. P. van Dam, American Mathematical Society, Providence, R. I., 1991, pp. 237-247.

13. Dacles-Mariani, J., Rogers, S. E., Kwak, D., Zilliac, G., and Chow, J., "A Computational Study of Wingtip Vortex Flowfield," AIAA Paper No. 93-3010, 1993.

14. Chorin, A., J., "A Numerical Method for Solving Incompressible Viscous Flow Problems," *Journal of Computational Physics,* Vol. 2, pp. 12-26, 1967.

15. Beam, R. M., Warming, R. F., " An Implicit Factored Scheme for the Compressible Navier-Stokes Equations," *AIAA Journal* , Vol 16, pp. 393-401, 1978.

16. Roe, P.L., "Approximate Riemann Solvers, Parameter Vectors, and Difference Schemes," *Journal of Computational Physics,* Vol. 43, pp. 357-372 1981

17. Chakravarthy, S. R., Osher, S., "A New Class of High Accuracy TVD Schemes for Hyperbolic Conservation Laws," AIAA Paper No. 85-0363, 1985.

18. Rai, M. M. "Unsteady Three-Dimensional Navier-Stokes Simulations of Turbine Rotor-Stator Interaction," AIAA Paper No. 87-2058, 1987.

19. MacCormack, R., W., "Current Status of Numerical Solutions of the Navier-Stokes Equations," AIAA Paper No. 85-0032, 1985.

20. Baldwin, B., S. and Barth, T., J., "A One-Equation Turbulence Transport Model for High Reynolds Number Wall-Bounded Flows," AIAA Paper No. 91-0610, 1991.

21. Fusegi, T., and Farouk, B., "Predictions of Fluid Flow and Heat Transfer Problems by the Vorticity-Velocity formulation of the Navier-Stokes Equations," *J. Computational Physics*, Vol 65, PP 227-243, 1986.

Appendix A

Kiris, C. and Kwak, D., "Progress in Incompressible Navier-Stokes Computations for the Analysis of Propulsion Flows," NASA CP 3282, Vol II, Advanced Earth-to-Orbit Propulsion Technology, 1994.

Appendix B

Kiris, C. Rogers, S., Kwak, D., and Lee, Y. T., "Time-Accurate Incompressible Navier-Stokes Computations with Overlapped Moving Grids," ASME Fluids Engineering Summer Meeting, Lake Tahoe, Nevada, June 19-23, 1994.

Figure 1 : Hub surface colored by static pressure

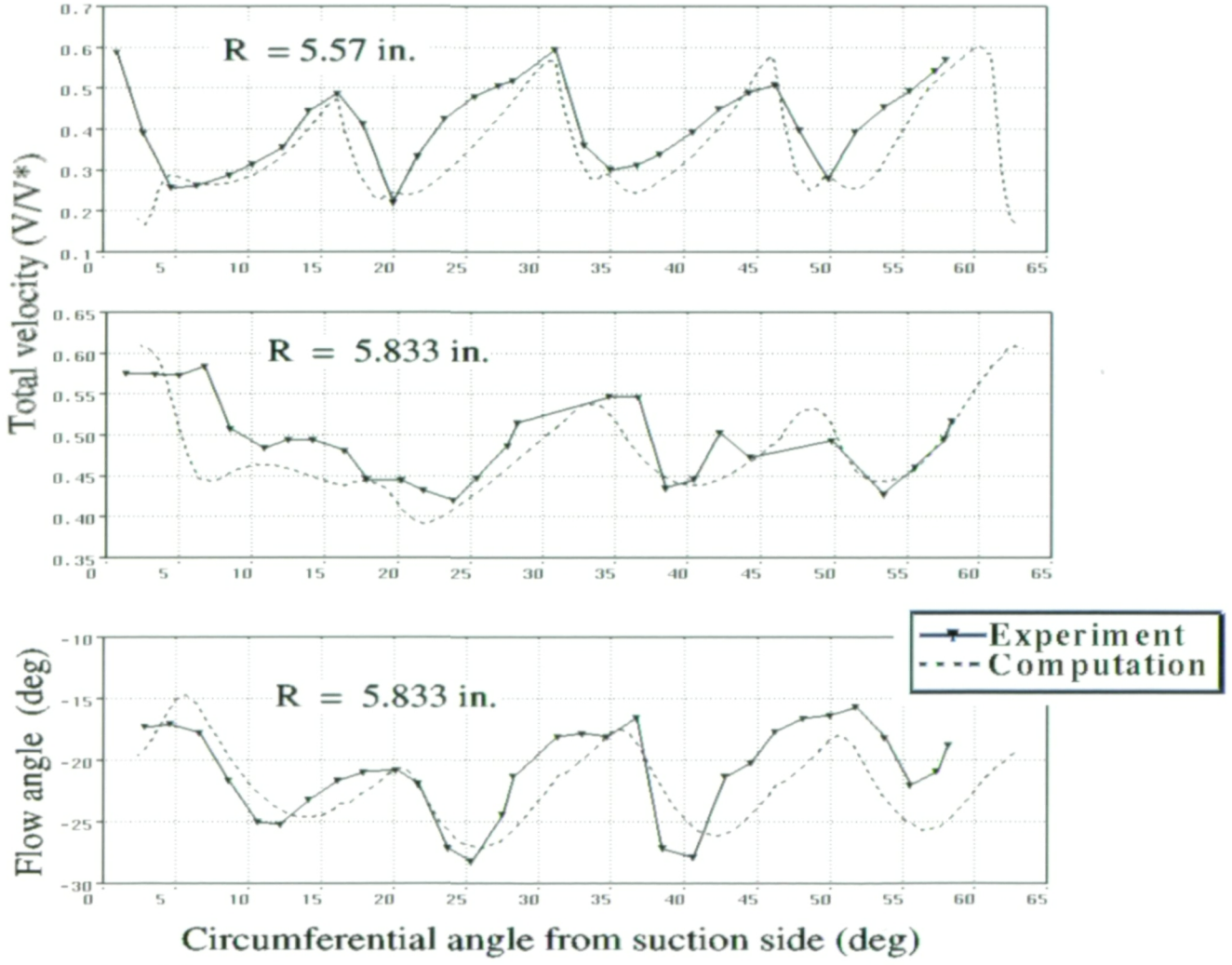

Figure 2 : Velocity and flow angle distributions downstream of SSME–HPFTP impeller exit plane (impeller exit radius : 5.5 in.)

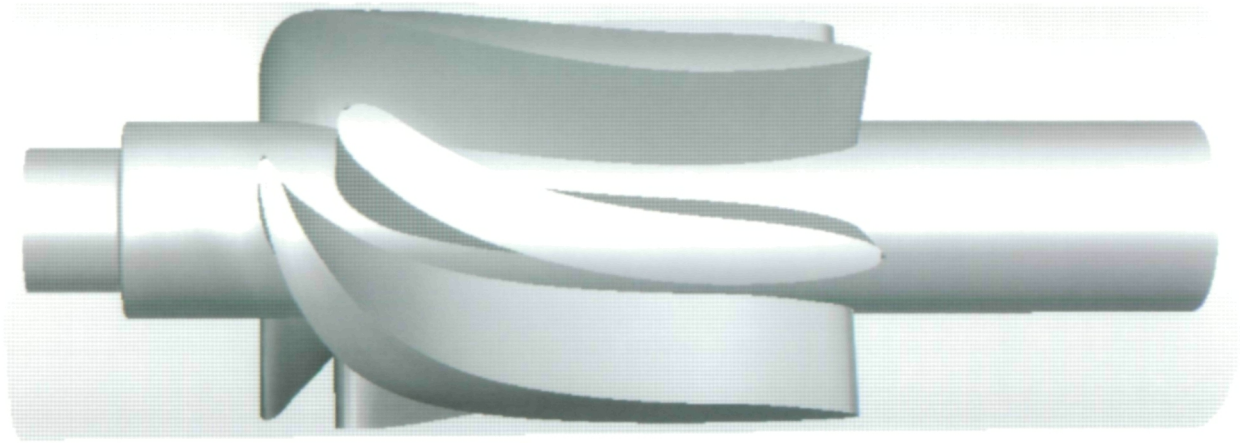

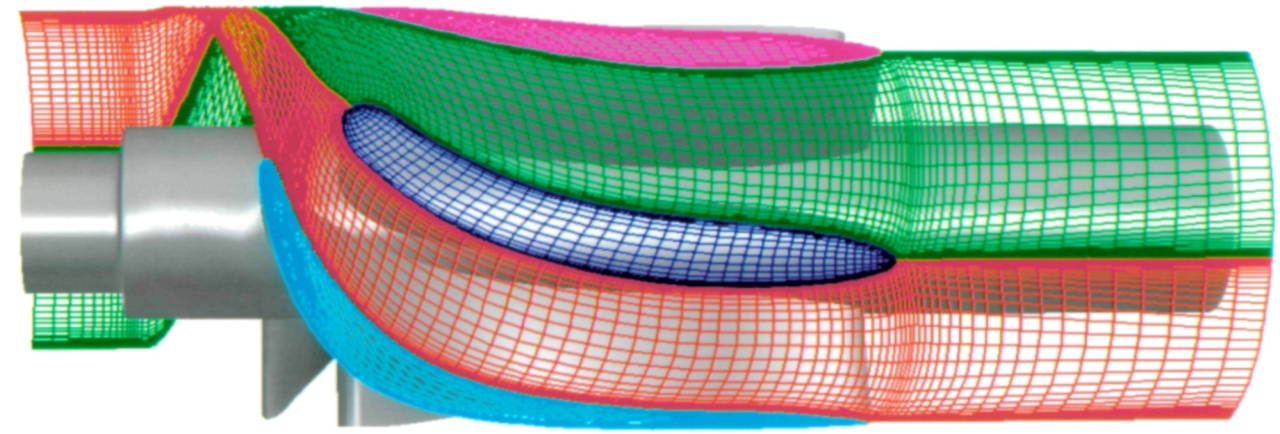

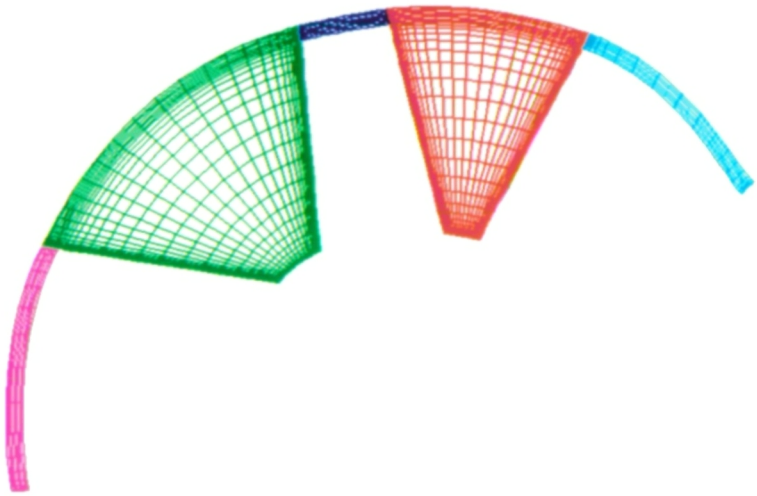

Zone 1 :127 x 39 x 33

Zone 2 :127 x 39 x 33

Zone 3 : 59 x 21 x 7

Zone 4 : 47 x 21 x 7

Zone 5 : 59 x 21 x 7

Figure 3 : Geometry and computational grid for the old design of the LVAD impeller

ORIGINAL PAGE
COLOR PHOTOGRAPH

ORIGINAL PAGE
COLOR PHOTOGRAPH

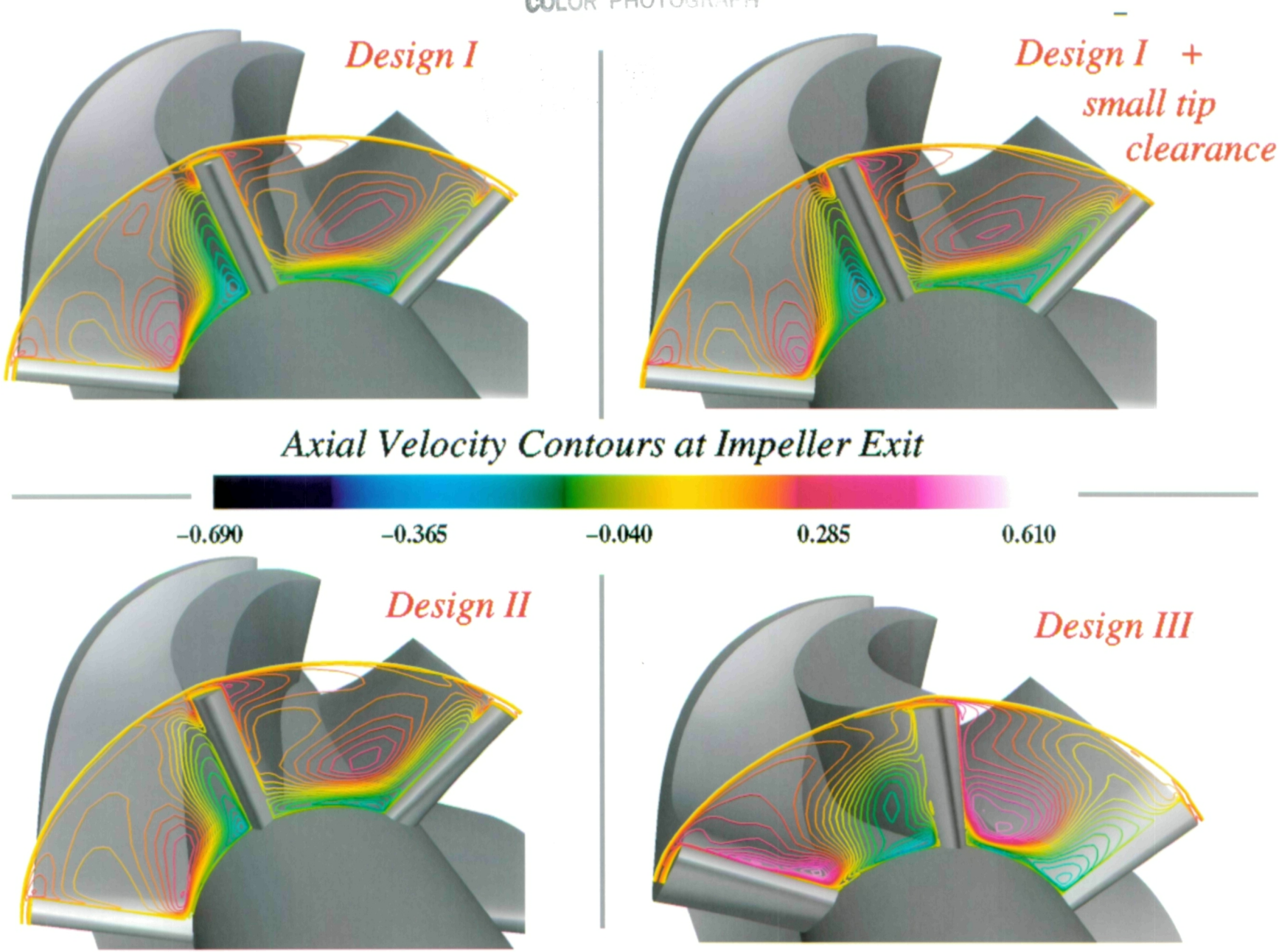

Figure 4 : Axial velocity contours at the exit plane of various LVAD impeller design

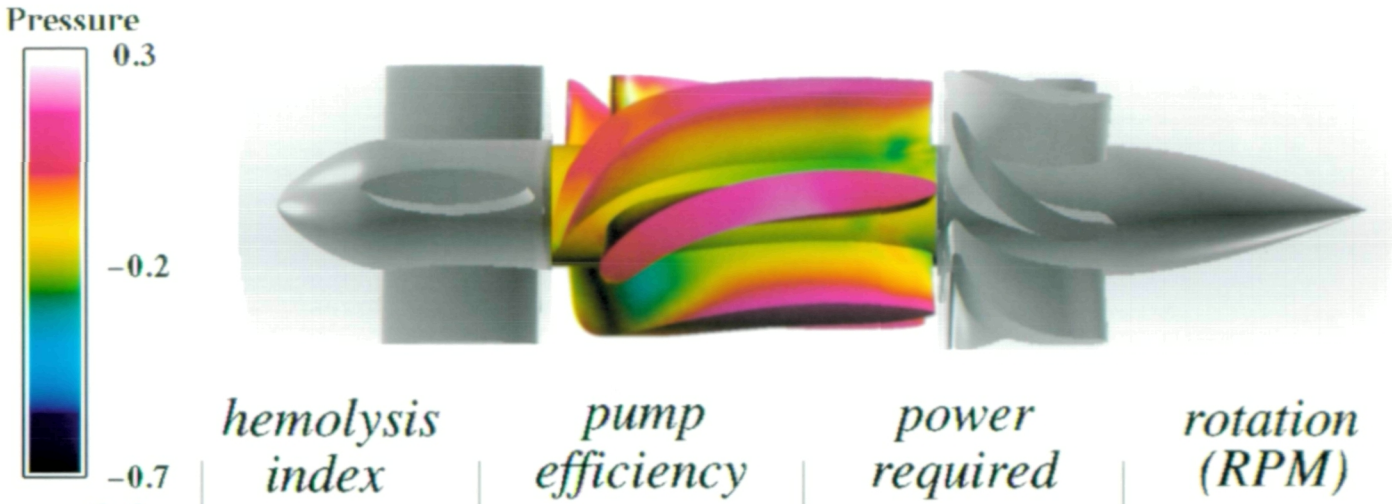

	hemolysis index	*pump efficiency*	*power required*	*rotation (RPM)*
old design	*0.02*	*0.25*	*12.6 watts*	*12,600*
new design	*0.002*	*0.33*	*9.8 watts*	*10,800*

Figure 5 : Hub and blade surfaces of the old and new designs of the LVAD impeller are colored by pressure. The table shows clinical results from BCOM

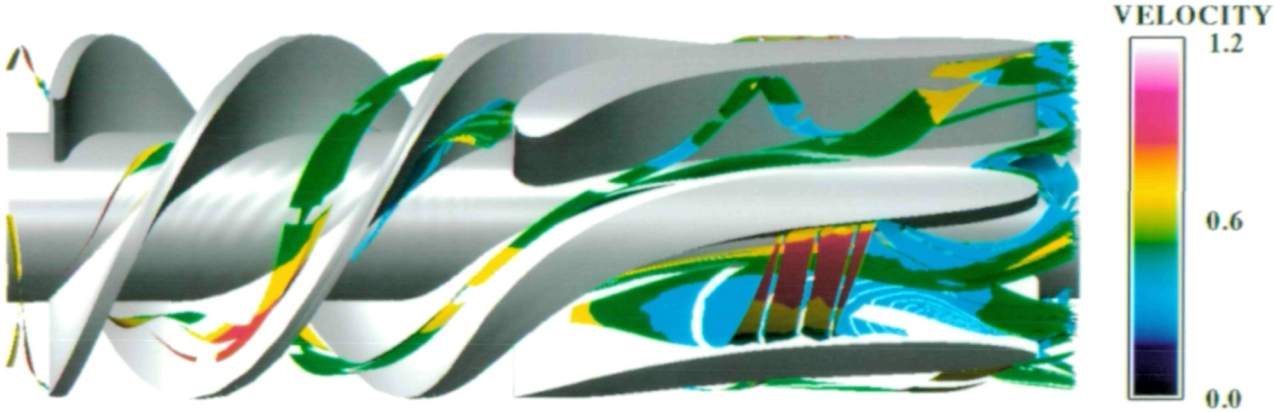

Figure 6 : Particle traces inside of the new design of the LVAD impeller are colored by velocity magnitude

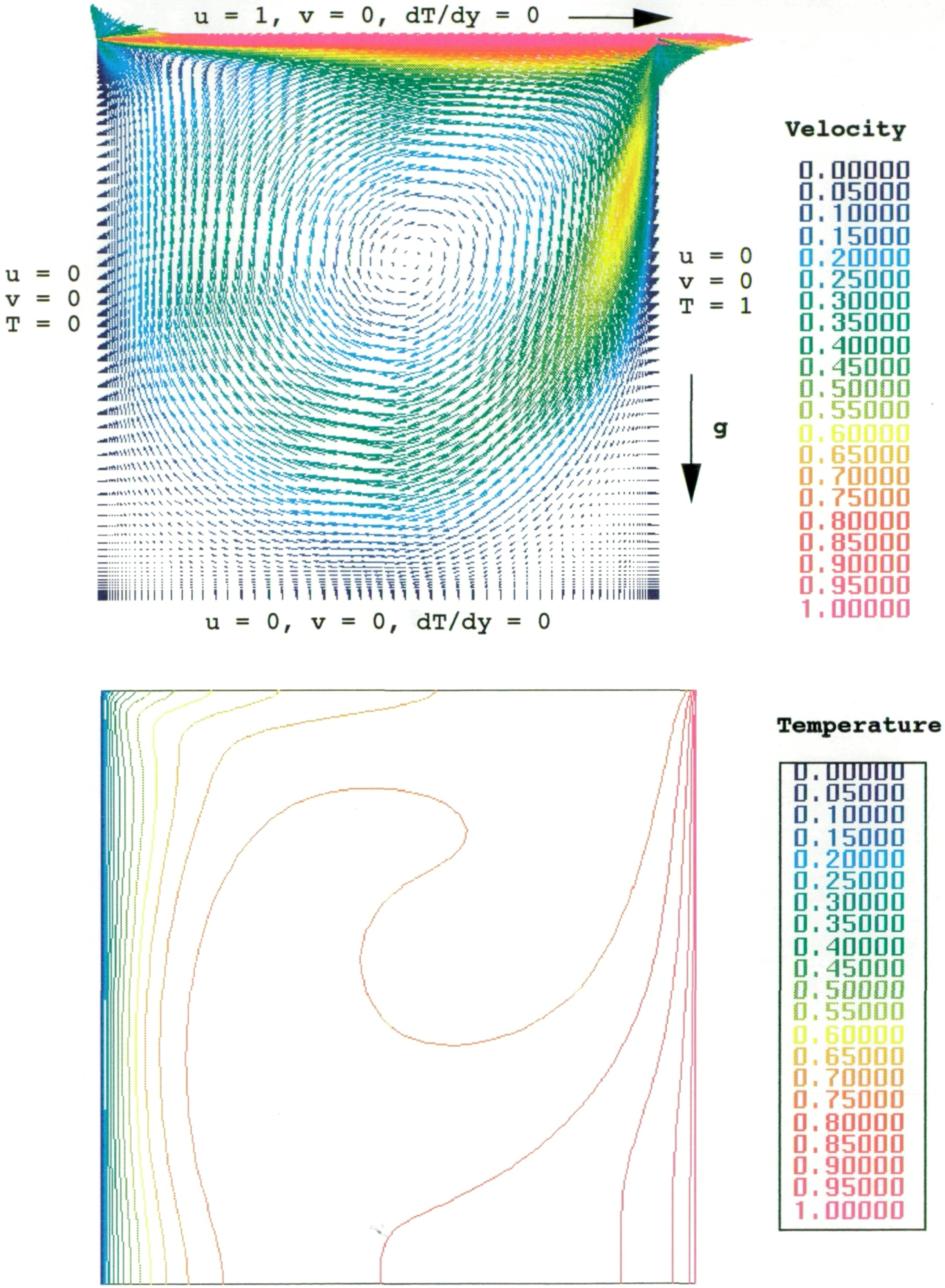

Figure 7 : Velocity vectors and temperature contours (forced convection, Re = 400)

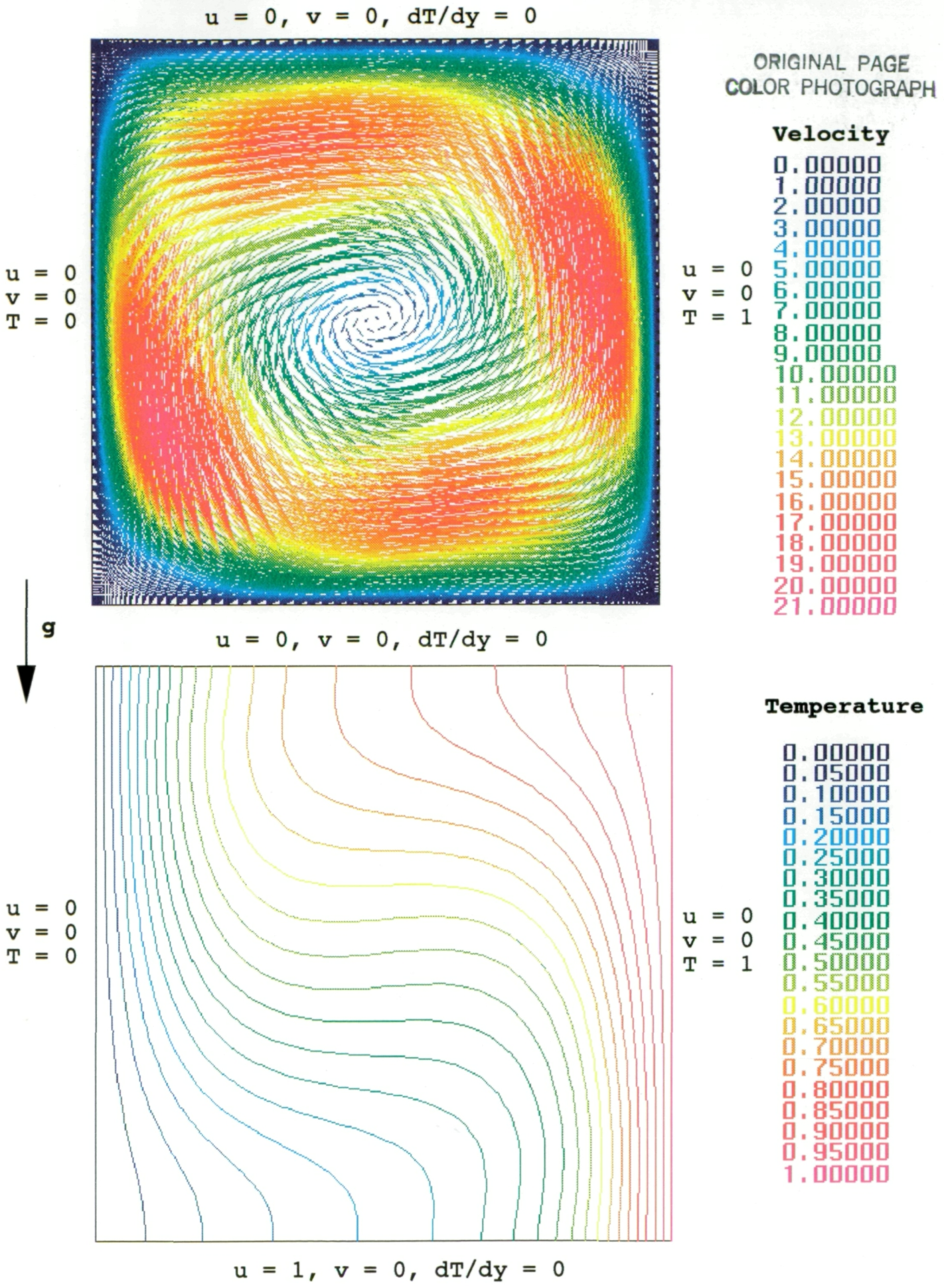

Figure 8 : Velocity vectors and temperature contours (natural convection, Ra = 10,000)

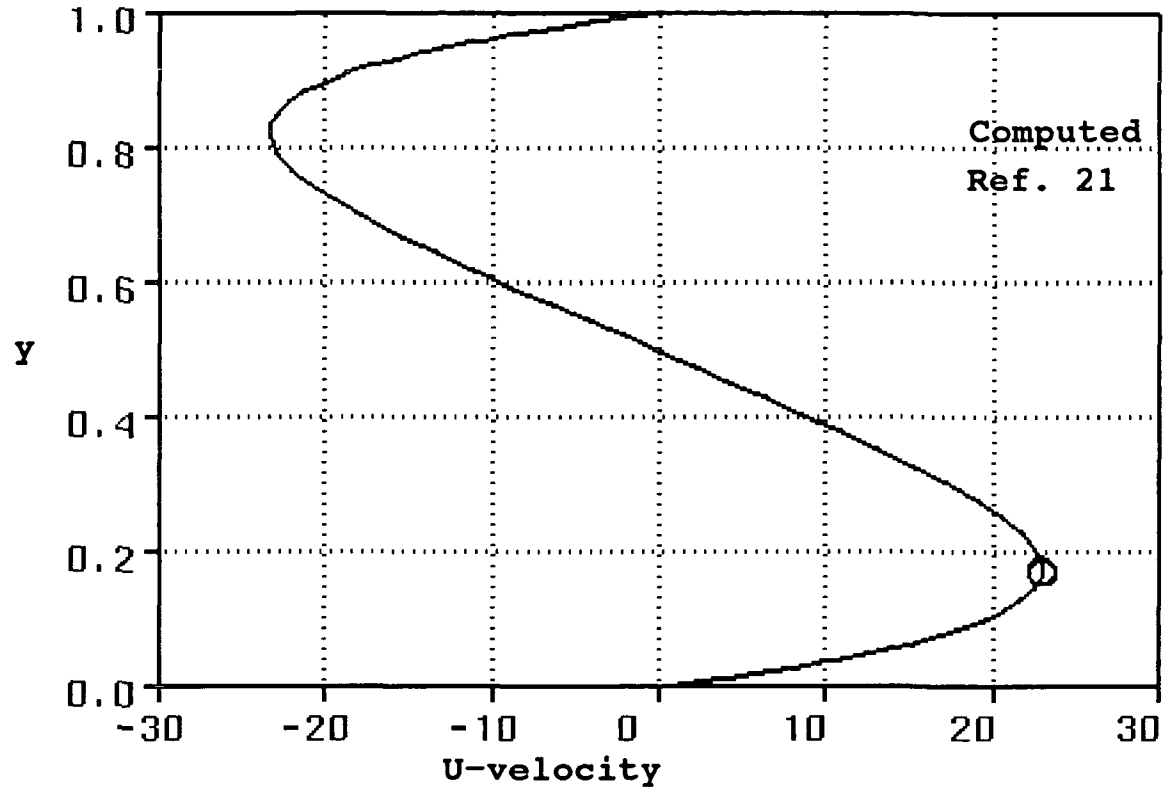

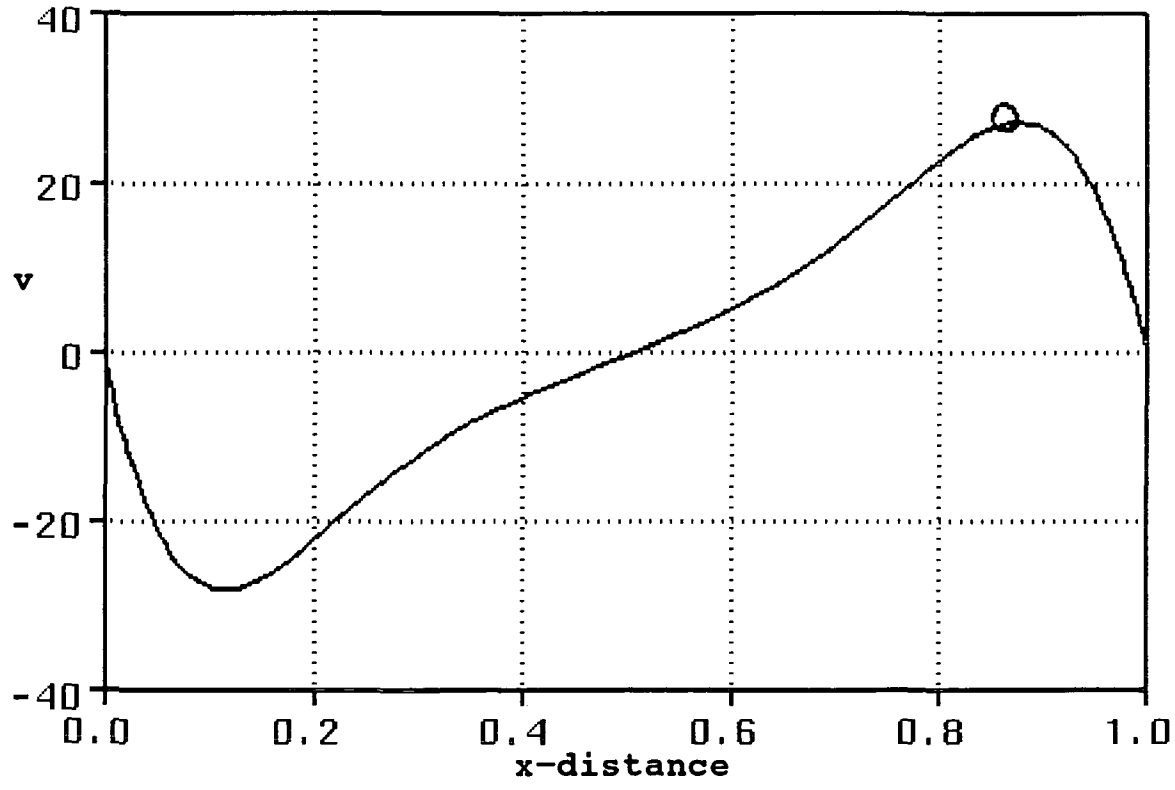

Figure 9 : Profiles of u- and v- velocity components along vertical and horizontal mid-planes (Ra = 10,000).

APPENDIX A

1994 Conference on
Advanced Earth-to-Orbit Propulsion Technology

NASA CP 3282

PROGRESS IN INCOMPRESSIBLE NAVIER-STOKES COMPUTATIONS FOR THE ANALYSIS OF PROPULSION FLOWS

Cetin Kiris*
MCAT Institute, Mountain View, CA

and

Dochan Kwak**
NASA-Ames Research Center, Moffett Field, CA

Abstract

Steady and unsteady flows for propulsion systems are efficiently simulated by solving the incompressible Navier-Stokes equations. The solution method is based on the pseudocompressibility approach and uses an implicit-upwind differencing scheme together with the Gauss-Seidel line relaxation method. Current computations use one-equation Baldwin-Barth turbulence model which is derived from a simplified form of the standard $k-\epsilon$ model equations. The resulting computer code is applied to the flow analysis inside an advanced rocket pump impeller in steadily rotating reference frames. Numerical results are compared with experimental measurements. The effects of exit and shroud cavities with the leakage flow are investigated. Time-accurate incompressible Navier-Stokes formulation with the overlapped grid scheme capability was evaluated by using MIT flapping foil experiment. The effects of grid density and of the order of differencing were investigated. The resulting procedure were applied to unsteady flapping foil calculations. Two upstream NACA 0025 foils perform high-frequency synchronized motion and generate unsteady flow conditions to the downstream larger stationary foil. Numerical results obtained from steady flow computations were compared against experimental data.

Introduction

Since the space launch systems in the near future are likely to rely on liquid rocket engines, increasing the efficiency and reliability of the engine components is an important task. One of the major problems in the liquid rocket engine is to understand the fluid dynamics of fuel and oxidizer flows. Understanding the flow in the turbopump through numerical simulation will be of significant value toward finding a better design that is simpler yet more efficient and robust with less manufacturing cost. Until recently, the pump design process was not significantly different from that of decades ago. The current semi-empirical turbomachinary design process does not account for the three-dimensional (3-D) viscous phenomena in the pump flows. Some of these 3-D viscous phenomena include wakes; the boundary layers in the hub, the shroud and the blades; junction flows; and tip clearence flows. In order to meet the challenge of improving propulsion devices, NASA Marshall Space Flight Center (MSFC) has established a consortium involving universities, industries, and NASA.[1-2]

Even though computational fluid dynamics (CFD) applications in turbines have been reported widely in the literature[3-5], the applications in the pump area are quite limited. The objective of this paper is to present, evaluate, and validate a computational procedure that solves incompressible Navier-Stokes equations for the pump components. For CFD to have an impact in the design procedure of the pump, a robust, efficient, and accurate scheme is required. In addition, the algorithm needs to be extensively validated for the flow-through pump components so that pump designers have the confidence to use it. The present work is focused on steady-state component analyses to validate the algoritm with a one-equation turbulence model and to demonstrate the code capability. For the pump components, such as an inducer and a radial impeller, the steady flow assumption is valid without the diffuser and inlet guide vanes. The progress in unsteady pump flows will be reported in the future. An effort similar to the present work can be seen in the activities of the other members of the MSFC Pump Stage Technology (PST) team.[6-8] Their formulations are based on a pressure based method and the current formulation is based on a pseudocompressibility method.

The numerical solution of the incompressible Navier-Stokes equations requires special attention in order to satisfy the divergence-free constraint on the velocity field because the incompressible formulation does not yield the pressure field explicitly from the equation of state or through the continuity equation. One way to avoid the numerical difficulty originated by the elliptic nature of the problem is to use a pseudocompressibility method. With the pseudocompressibility method, the elliptic-parabolic type equations are transformed into hyperbolic-parabolic type equations. Well established solution algorithms developed for compressible flows can be utilized to solve the resulting equations. Steger and Kutler[9] employed an alternating-direction implicit scheme into Chorin's[10]

* Research Scientist
** Branch Chief

pseudocompressibility method. This formulation was extended to three-dimensional generalized coordinates by Kwak and Chang.[11,12] Recently, a three-dimensional incompressible Navier-Stokes solver[13] (INS3D-UP) that uses upwind differencing and the Gauss-Seidel line relaxation scheme was developed in order to have a robust and fast-converging scheme. The flow over single and multi-element airfoils was simulated efficiently by using this algorithm.[14] A time-accurate formulation of the algorithm is implemented for incompressible flows through artificial-heart devices with moving boundaries.[15] The present study is a continuation of the validation effort for the turbulent flow in rotating machinery in a steadily rotating frame of reference. Preliminary results from a benchmark case for the marine propulsors are also included in this paper.

In the following sections, the governing equations and the method of solution are summarized. and the computed results obtained from the current approach are presented.

Algorithm

The pseudocompressibility algorithm introduces a time derivative of the pressure term into the continuity equation. The resulting incompressible Navier-Stokes equations can be written in a generalized curvilinear coordinate system (ξ, η, ζ) as follows

$$\frac{\partial Q}{\partial \tau}+\frac{\partial}{\partial \xi}(E-E_v)+\frac{\partial}{\partial \eta}(F-F_v)+\frac{\partial}{\partial \zeta}(G-G_v) = S \quad (1)$$

where Q and the convective flux vectors E, F, G are

$$Q = \frac{1}{J}\begin{bmatrix} p \\ u \\ v \\ w \end{bmatrix}$$

$$E = \frac{1}{J}\begin{bmatrix} \beta U \\ \xi_x p + uU + \xi_t u \\ \xi_y p + vU + \xi_t v \\ \xi_z p + wU + \xi_t w \end{bmatrix}$$

$$F = \frac{1}{J}\begin{bmatrix} \beta V \\ \eta_x p + uV + \eta_t u \\ \eta_y p + vV + \eta_t v \\ \eta_z p + wV + \eta_t w \end{bmatrix}$$

$$G = \frac{1}{J}\begin{bmatrix} \beta W \\ \zeta_x p + uW + \zeta_t u \\ \zeta_y p + vW + \zeta_t v \\ \zeta_z p + wW + \zeta_t w \end{bmatrix}$$

Here J, β, p, u, v, and w denote the Jacobian of transformation, the pseudocompressibility coefficient, pressure, and cartesian velocity components, respectively. The contravariant velocity components U, V, and W are defined as

$$U = \xi_x u + \xi_y v + \xi_z w$$
$$V = \eta_x u + \eta_y v + \eta_z w$$
$$W = \zeta_x u + \zeta_y v + \zeta_z w$$

The viscous fluxes, E_v, F_v, and G_v, are given by

$$\hat{E}_v = \frac{1}{ReJ}\begin{bmatrix} (\nabla\xi\cdot\nabla\xi)u_\xi + (\nabla\xi\cdot\nabla\eta)u_\eta + (\nabla\xi\cdot\nabla\zeta)u_\zeta \\ (\nabla\xi\cdot\nabla\xi)v_\xi + (\nabla\xi\cdot\nabla\eta)v_\eta + (\nabla\xi\cdot\nabla\zeta)v_\zeta \\ (\nabla\xi\cdot\nabla\xi)w_\xi + (\nabla\xi\cdot\nabla\eta)w_\eta + (\nabla\xi\cdot\nabla\zeta)w_\zeta \end{bmatrix}$$

$$\hat{F}_v = \frac{1}{ReJ}\begin{bmatrix} (\nabla\eta\cdot\nabla\xi)u_\xi + (\nabla\eta\cdot\nabla\eta)u_\eta + (\nabla\eta\cdot\nabla\zeta)u_\zeta \\ (\nabla\eta\cdot\nabla\xi)v_\xi + (\nabla\eta\cdot\nabla\eta)v_\eta + (\nabla\eta\cdot\nabla\zeta)v_\zeta \\ (\nabla\eta\cdot\nabla\xi)w_\xi + (\nabla\eta\cdot\nabla\eta)w_\eta + (\nabla\eta\cdot\nabla\zeta)w_\zeta \end{bmatrix}$$

$$\hat{G}_v = \frac{1}{ReJ}\begin{bmatrix} (\nabla\zeta\cdot\nabla\xi)u_\xi + (\nabla\zeta\cdot\nabla\eta)u_\eta + (\nabla\zeta\cdot\nabla\zeta)u_\zeta \\ (\nabla\zeta\cdot\nabla\xi)v_\xi + (\nabla\zeta\cdot\nabla\eta)v_\eta + (\nabla\zeta\cdot\nabla\zeta)v_\zeta \\ (\nabla\zeta\cdot\nabla\xi)w_\xi + (\nabla\zeta\cdot\nabla\eta)w_\eta + (\nabla\zeta\cdot\nabla\zeta)w_\zeta \end{bmatrix}$$

where Re is the Reynolds number.

When the equations are solved in steadily rotating reference frames, the centrifugal force and the Coriolis force terms are added to the equation of motion as source terms. If the relative reference frame is moving around the $x-$ axis, the source term S is given by

$$S = \begin{bmatrix} 0 \\ 0 \\ \Omega(\Omega y + 2w) \\ \Omega(\Omega z - 2v) \end{bmatrix}$$

where Ω is the rotational speed. Both the viscous and source terms are treated implicitly in the numerical formulation. Relative velocity components are written in terms of absolute velocity components u_a, v_a, and w_a as

$$u = u_a$$
$$v = v_a + \Omega z$$
$$w = w_a - \Omega y$$

In the steady-state formulation, the time derivatives are differenced using by the Euler backward formula. The equations are solved iteratively in pseudo-time until the solution converges to a steady state. Central differencing is used to compute the viscous flux derivatives and third-order upwind differencing is employed to compute the convective flux derivatives. Chakravarthy[16] outlines a class of high-accuracy flux-differencing schemes for the compressible flow equations. Following Chakravarthy's third-order scheme, a fifth-order-accurate, upwind-biased stencil was derived by Rai.[3] The upwind differencing used here is an implementation of those efforts for the incompressible Navier-Stokes equations. For the computations presented in this paper, third-order flux-differencing scheme is used.

An implicit, delta-law form approximation to equation (1) after linearization in time and the use of approximate Jacobians of the flux differences result in a

seven-block diagonal matrix equation written as

$$\bar{B}\delta Q_{i-1,j,k} + \bar{A}\delta Q_{i,j,k} + \bar{C}\delta Q_{i+1,j,k} + \bar{D}\delta Q_{i,j-1,k} + \bar{E}\delta Q_{i,j+1,k} + \bar{F}\delta Q_{i,j,k-1} + \bar{G}\delta Q_{i,j,k+1} = R.H.S. \quad (2)$$

where $\delta Q = Q^{n+1} - Q^n$ and $\bar{A}, \bar{B}, \bar{C}, \bar{D}, \bar{E}, \bar{F}$, and $\bar{G}$ are 4 x 4 block diagonals.

The Gauss-Seidel line relaxation scheme, which was successfully employed by MacCormack[17], is used to solve this matrix equation. In equation (2), the right-hand-side term is computed and stored for the entire domain. In the present study, the line-relaxation procedure is composed of three stages; each stage involves a block-tridiagonal inversion in one direction. Fig 1 shows the block tridiagonal inversion lines and the Gauss-Siedel sweep planes for the three directions. In the first stage, δQ is solved line by line in one direction. Before the block-tridiagonal equation is solved, off-tridiagonal terms are multiplied by the current value of δQ and then shifted over to the right-hand-side of the equation. In other words, equation (2) is solved by performing a block-tridiagonal inversion in the $\xi-$direction and Gauss-Seidel sweeps in the $\eta-$ and $\zeta-$directions. The second stage is to solve the block-tridiagonal terms in the $\eta-$ direction, and to perform backward and forward sweeps in the $\zeta-$ and $\xi-$directions. The same procedure is repeated in the third stage by inverting the block-tridiagonal matrix in the $\zeta-$direction, and treating the off-diagonal terms for the $\xi-$ and $\eta-$directions in Gauss-Seidel fashion. After the first sweep is completed for the entire domain, a backward sweep is started in the opposite direction. One forward sweep and one backward sweep for each computational direction are sufficient for most problems, but the number of sweeps can be increased.

Implicit boundary conditions are used at all the boundaries except the zonal interface boundaries; zonal interface boundaries are updated quasi-implicitly, a method very suitable for the line-relaxation scheme. The change in the dependent variables for one time-step is passed during line-relaxation sweeping from one zone to another. Nonslip boundary conditions are imposed at the solid stationary wall. The pressure boundary condition is specified such that the pressure gradient normal to the wall is zero. At the inflow and outflow boundaries, characteristic boundary conditions are employed implicitly. It is assumed that the effect of viscous terms at the boundaries is negligible. Also, the characteristic equations are approximated in one-dimensional space. The primitive variables that are needed at the boundaries are the pressure p and the velocity components u, v, w. The number of positive and negative eigenvalues of the Jacobian matrix of the convective flux determines how many variables should be specified at the boundaries. If the flow is in the positive $\xi-$direction, then there will be three characteristic waves traveling downstream and one characteric wave traveling upstream. The exit boundary receives the information about the three variables via the characteristics traveling from the interior of the domain. Hence, only one variable is specified at the outflow boundary. However, the inflow boundary receives only one characteristic traveling from the interior region, and, therefore, three variables are specified at the inflow boundary. For the calculations presneted in this report, u, v and w velocities were specified at the inflow and static pressure was specified at the outflow. Details of the numerical method are given in reference 13.

The present calculations use the one-equation turbulence model developed by Baldwin and Barth.[18] The transport equation for the turbulent Reynolds number is derived from a simplified form of the standard $k-\epsilon$ model equations. The model is relatively easy to implement because there is no need to define an algebraic length scale. The formulation and code issues can be found in reference 18. The transport equation is also solved by using a Gauss-Seidel type line relaxation scheme.

Pump Components

The flowfield through a turbopump inducer geometry as shown in figure 2 was solved as a benchmark problem for turbomachinery applications. An inducer that provides a sufficient pressure rise to the flow in order to prevent the cavitation on impeller blades is a crucial element of a rocket engine pump. The design flow of the Rocketdyne inducer is 2236 gallons per minute (gal/min) and, the design speed is 3600 revolutions per minute (rpm). In the computational study, tip-leakage effects are included with a tip clearance of 0.008 inches (in). The Reynolds number for this calculation was 191,800 per inch. The solution was considered converged when the maximum residual dropped at least five orders of magnitude. The convergence history is shown in figure 3. Computer time required per grid point per iteration was about 1.5 x 10^{-4} seconds (sec). The surfaces of the inducer hub and blades are colored by nondimensionalized pressure in figure 4. The pressure is nondimensionalized by ρV^2, where ρ is the density and V is the average inflow velocity. The pressure gradient across the blades due to the action of centrifugal force and the pressure rise from inflow to outflow are shown. Figure 5 shows the particle traces colored by relative total-velocity magnitude. The particles were released near the hub, the blade suction side, and the tip regions, and then the traces were calculated from the relative velocity field. Near the hub, the particles rise up in the boundary layer and move from the pressure side to the suction side of the blade. The swirling motion of the particles indicates a secondary flow region near the hub. The particles released near the suction side of the blade indicate a radial velocity component inside the blade boundary

layer because low energy fluid is controlled by centrifugal force. The particles tend to flow from the hub suction side to the tip suction side of the blade. The particles near the casing show an opposite trend from the ones near the hub. Since the casing has counterrotating wheel speed in the relative frame of reference, the particles move from the suction side to the pressure side. The structure of the internal turbulent flow in the present configuration is quite complicated. The comparison between numerical results and exerimental measurements was presented in reference 19. The comparison showed that the solution algorithm does a reasonably good job. The existing solution procedure can be applied to a similar configuration in off-design conditions. Such a numerical study could potentially predict cases in which the inducer may suffer from massive separation and result in a blocked fuel supply. The numerical study can provide the designer a safe operating envelope of a particular inducer. This is the future research area of this study which can be used in the predesign and postdesign engineering tool in challenging turbomachinery applications.

The current procedure was applied in a flow analysis inside an advanced pump-impeller geometry to verify the design. Comparison between the computed results and experimental measurments was presented in reference 20. The impeller design flow is 1,205 gal/min with a design speed of 6,322 rpm. The Reynolds Number for this calculation was 181,273 per inch. Figure 6 shows the computational grid near the hub region of the impeller. The results with vaneless space and without the vaneless space show the effect of downstream conditions. Figures 7-a and 7-b show the meridional velocity distribution at the impeller discharge. A relative x-distance is measured from the shroud to the hub, where $x = 1.0$ is the hub. The meridional velocities, CM, were integrated along a radial strip for each constant $x-$position and they were nondimensionalized by the wheel tip speed of 249.5 ft/sec. In figure 7-a, the dashed line represents CM distributions for the flow without vaneless space. The solid line denotes the CM distributions for the flow with vaneless space. The effect of downstream boundary conditions can be seen by comparing the solid line with the dashed line in figure 7-a. In case where the vaneless space is not included, the flow is pumped near the hub and shroud regions, and the velocity profile is flattened in the core region. The meridional velocity distributions for 5% and 10% recirculation from the exit shroud cavity were also plotted in figure 7-b. When the shroud cavity has leakage to the impeller eye, the velocity peak at the impeller exit moves toward to the center of the B2 width. However, the effect of the shroud leakage has minor effects on the solution at $r/rtip = 1.0275$ (figures 7-b and 8). In figure 7-b, the symbols represent experimental data[21], and the lines represent CM distributions for the flow with vaneless space. When the vaneless space is included, the velocity profile shows a peak at approximately 60% of the B2 width. The test data shows that the peak is closer to the center of the B2 width. The discrepency between the computed results and experimental data is partially due to the recirculation flow in the hub cavity. The leakage at the hub cavity leads to stronger recirculation region which shifts the velocity peak to the center of B2 width. Since the CFD analysis did not include the leakage at the hub cavity, the predicted recirculation region in the vaneless space is not as strong as in the experimental study. Figure 8 shows blade-to-blade velocity distributions at the impeller exit. The jet-wake pattern was captured at all three axial locations. The numerical results compare fairly well with the experimental data.

MIT Flapping Foil Experiment
Part-I: Steady Flow

The purpose of the MIT flapping foil experiment (FFX) is to provide detailed unsteady measurements for CFD code validations for marine propulsors. The FFX was designed as a two-dimensional representation of the interaction between the propeller-blade and wake flows.[22] A schematic of the experimental set-up is given in figure 9. The stationary foil represents a propeller blade embedded in a wake flow generated by upstream pitching foils. The stationary foil has an 18-inch chord and a 1.18 degree angle-of-attack. The upstream flapping foils are NACA 0025 foils of 3-inch chord. The flappers perform synchronized sinusoidal motions of 6-degree amplitude at a reduced frequency of 3.62. The flappers in the FFX generate periodic wake fluctuations which impose an unsteady condition on the stationary foil. Velocity and pressure measurements at a Reynolds number (based on the stationary foil chord and the inflow mean velocity) of 3.78×10^6 were taken on and around the stationary foil inside the measurement box, which is shown by the dashed line in figure 9. Previous computations of the FFX include the following: a simplified configuration for the FFX was numerically simulated using a potential flow formulation;[23] a patched, time-varying, multiblock grid system was employed with a pseudocompressibility formulation by researchers at Mississippi State University[24] to simulate the FFX configuration; a chimera overlaid-grid scheme with a pressure-based method was used in the FFX simulation by Peterson and Stern.[25] In this paper, the results from steady flow calculations are presented. Since experimentally measured data was available for steady flow with stationary flappers with zero degree angle of attack, steady-state calculations were carried out to validate the current approach before starting the more time consuming time-dependent calculations. Unsteady flapping foil calculations will be presented in reference 26.

The grid topology for the FFX is shown in figure 10. An H-type grid with the dimension of 253x191

(grid 1) occupies the water tunnel without considering the foils. Three C-type grids are generated for the foils and are overlapped with the tunnel grid. Grid 2 is generated for the stationary foil with the grid dimension of 337x61. Grids 3 and 4 wrap around the flappers with the grid dimension of 215x40. The total number of grid points for this grid system is 86080. The individual grids receive information from each other by interpolating the dependent variables. The grids around the foils have outer boundaries which overlap the interior region of the tunnel grid. The tunnel grid has an interior boundary surrounding a hole. A hole point is a mesh point which is removed from the solution procedure. The immediate neighbor points of the hole points are called fringe points and are updated from the interpolation procedure.

Figure 11 compares the measured and calculated static pressure coefficient (Cp) on the stationary foil surface. The symbols represent the experimental measurements, and the lines represent the computed results. All numerical results show very good agreement with the measured data. Figures 12 through 14 show the velocity profiles at several streamwise locations on the surfaces and at the wake of stationary foil. These profiles plot the magnitude of the component of velocity that is tangential to the local stationary foil surface. Symbols represent the experimental measurements and the solid lines represent numerical results obtained by using the overlapped grid topology. Figures 12 through 14 indicate that the computed results compare very well with the measured data at the boundary layer and the wake of the stationary foil. The biggest discrepancy between the computed results and the measured data is seen in the wake of the foil (x/c=1.2). The velocity at the edge of the wake is overpredicted with less then a couple of percent error range. In order to make sure the steady flow results are grid independent, some additional computations were carried out. The order of accuracy for convective terms in coarse grid calculations was increased from third-order to fifth-order flux difference splitting. The third-order coarse grid result is shown with the dashed line and the fifth-order coarse grid result is shown with the chaindashed line in figure 15. The solid line and the dotted line with x-marks represent the fine grid third-order and fifth-order results, respectively. The wake from the fine grid computations clearly show better agreement than the coarse grid does with the measured data. The overshoot which occurs at the edge of the wake in the third-order results does not occur in the fifth-order results. In the finest grid computations, the base grid for the stationary foil was refined by increasing the number of grid points in the normal direction from 61 to 91. The velocity profile from the resulting finer grid (total 97K points) with the third-order differencing is plotted with the chaindotted line. This fine grid result is very similar to the base grid (86K grid point) result, indicating that this is close to grid independent solution and that 86K point grid will provide adequate resolution for the unsteady calculations. In fact, the difference between the 86K and the 97K grid results is less than the oscillations in the measured data. Notethat there is a rather large differencing between the measured and computed wake edge velocities. Since this edge velocity is shown to be grid independent, it is thought that the experimental data used an erroneous value for the reference velocity for this data. In addition, all computed results have the same velocity magnitude at the edge of the wake and fine grid results are self consistent. Because of these reasons, the result shown with solid line in figure 15 is considered to be a reasonably grid independent solution. At this point, it is believed that the computational procedure is ready for the unsteady flapping foil calculations which are currently underway. Results from the unsteady calculations will be repoted in reference 26.

Conclusions

An efficient and robust solution procedure for 3-D pump component analyses has been presented. The technique solves the viscous incompressible Navier-Stokes equations with source terms in a steadily rotating reference frame. The method of pseudocompressibility with higher-order accurate upwind differencing and a Gauss-Seidel line relaxation scheme are utilized. The flow through a pump inducer and an impeller have been successfully simulated. Numerical results from a one-equation Baldwin-Barth turbulence model compare fairly well with experimental data.

A detailed study for the steady-state MIT flapping foil calculations was performed to investigate the effects of grid resolution, and the order of accuracy. The one-equation Baldwin-Barth turbulence model was able to accurately compute the Cp and boundary layer velocity distribution on the stationary airfoil. A nearly grid independent solution was obtained for the steady FFX simulation by using third-order flux-difference splitting for the convective terms. Overall, the computed steady-state results showed good agreement with the experimentally measured Cp and boundary layer profiles on on the stationary foil.

Acknowledgments

This work was partially supported by NASA Marshall Space Flight Center. The work of the first author was supported by NASA Ames Research Center through Cooperative Agreement NCC 2-500. Computer time was provided by the Numerical Aerodynamic Simulation (NAS) Facility and the Central Computing Facility at NASA Ames Research Center. The authors would like to thank Mr. Roberto Garcia of

MSFC for postprocessing the advanced impeller calculations.

References

[1] Garcia, R., Jackson, E.D., and Schutzenhofer, L.A., "A Summary of the Activities of the NASA/ MSFC Pump Stage Technology Team," Proceedings of the Fourth International Symposium on Transport Phenomena and Dynamics of Rotating Machinery, April 5-8 1992, Honolulu, Hawaii.

[2] Garcia, R., McConnaughey, P., and Eastland, A., "Activities of MSFC Pump Stage Technology Team," AIAA Paper No. 92-3232, 1992.

[3] Rai, M. M. "Unsteady Three-Dimensional Navier-Stokes Simulations of Turbine Rotor-Stator Interaction," AIAA Paper No. 87-2058, 1987.

[4] Giles, M. B. "Generalized Conservation Cells for Finite Volume Calculations," AIAA Paper No. 87-1118, 1987.

[5] Giles, M. B. "Stator/Rotor Interaction in a Transonic Turbine," AIAA Paper No. 88-3093, 1988.

[6] Hah, C., Brayns, A.C., Moussa, Z., and Tomsho, M. E., "Application of Viscous Flow Computations for Aerodynamic Performance of a Backswept Impeller at Viscous Operating Conditions," J. of Turbomachinary, Trans. ASME, Vol. 110, pp. 303-311, July 1988.

[7] Chen, Y. S., "Compressible and Incompressible Flow Computations with a Pressure Based Method," AIAA Paper No. 89-0286, 1989.

[8] Chen, W. C., Pruger, G., Chen, D., and Eastland, A., "On the Use of a Three-Dimensional Navier-Stokes Solver for Rocket Pump Impeller Design," AIAA Paper No. 92-3223, 1992.

[9] Steger, J. L., Kutler, P., "Implicit Finite-Difference Procedures for the Computation of Vortex Wakes," *AIAA Journal*, Vol 15, no. 4, pp. 581-590, 1977.

[10] Chorin, A., J., "A Numerical Method for Solving Incompressible Viscous Flow Problems," *Journal of Computational Physics*, Vol. 2, pp. 12-26, 1967

[11] Kwak, D., Chang, J. L C., Shanks, S. P., and Chakravarthy, S., "A Three-Dimensional Incompressible Navier-Stokes Flow Solver Using Primitive Variables," *AIAA Journal*, Vol 24, no. 3, pp. 390-396, 1977.

[12] Chang, J., Kwak, D., Rogers, S. E., and Yang, R.-J., "Numerical Simulation Methods of Incompressible Flows and an Application to the Space Shuttle Main Engine," *Int. J. Num. Meth. in Fluids*, Vol 8, pp. 1241-1268, 1988.

[13] Rogers, S. E., Kwak, D. and Kiris, C., "Numerical Solution of the Incompressible Navier-Stokes Equations for Steady and Time-Dependent Problems," *AIAA Journal*, Vol 29, No 4, pp. 603-610, 1991.

[14] Rogers, S. E., Wiltberger, N. L., and Kwak, D. "Efficient Simulation of Incompressible Viscous Flow Over Single and Multi-Element Airfoils," AIAA Paper No. 92-0405, 1992.

[15] Kiris, C., Rogers, S. E., Kwak, D. and Chang, I. "Computation of Incompressible Viscous Flows through Artificial Heart Devices with Moving Boundaries," Fluid Dynamics in Biology, Proceedings of an AMS-IMS-SIAM Joint Research Conference, edited by A. Y. Cheer and C. P. van Dam, American Mathematical Society, Providence, R. I., 1991, pp. 237-247.

[16] Chakravarthy, S. R., Osher, S., "A New Class of High Accuracy TVD Schemes for Hyperbolic Conservation Laws," AIAA Paper No. 85-0363, 1985.

[17] MacCormack, R., W., "Current Status of Numerical Solutions of the Navier-Stokes Equations," AIAA Paper No. 85-0032, 1985.

[18] Baldwin, B., S. and Barth, T., J., "A One-Equation Turbulence Transport Model for High Reynolds Number Wall-Bounded Flows," AIAA Paper No. 91-0610, 1991.

[19] Kiris, C., Chang, L., Kwak, D., and Rogers, S., "Incompressible Navier-Stokes Computations of Rotating Flows," AIAA Paper No. 93-0678, 1993.

[20] Garcia, R., McConnaughey, P., and Eastland, A., "Computational Fluid Dynamics Analysis for the Reduction of Impeller Discharge Flow Distortion," AIAA Paper No. 94-0749, 1994.

[21] Brozowski, L. A., Ferguson, T.V., and Rojas, L., "Impeller Flow Field Lacer Velocimeter Measurements," Proceedings of the Fifth International Symposium on Transport Phenomena and Dynamics of Rotating Machinery, May 9-11, 1994, Kuanupulu, Maui.

[22] Kerwin, J., Keenan, D., Maxel, C., Horwich, E., and Knapp, M., "MIT/ONR Flapping Foil Experiment," MIT/ONR FFX Workshop, David Taylor Model Basin, March 1993.

[23] Lee, Y. T., Feng, J., and Merkle, C. L., "Time-Dependent Inviscid Flow Analysis of Rotor-Stator Systems," Sixth Int. Conf. on Numerical Ship Hydrodynamics, August 2-5, 1993.

[24] Taylor, L. K., Busby, J. A., Jiang, M. Y., Arabashi, A., Sreenivas, K., and Whitfield, D. L., "Time Accurate Incompressible Navier-Stokes Simulation of the Flapping Foil Experiment," Sixth Int. Conf. on Numerical Ship Hydrodynamics, August 2-5, 1993.

[25] Paterson, E., Stern, F., "Computation of Unsteady Viscous Flow with Application to the MIT Flapping-Foil Experiment," Sixth Int. Conf. on Numerical Ship Hydrodynamics, August 2-5, 1993.

[26] Kiris, C., Rogers, S., Kwak, D., and Lee, Y. T., "Time-Accurate Incompressible Navier-Stokes Computations with Overlapped Grids," Proceeding of the ASME Fluids Engineering Division Summer Meeting, June 10-23, 1994, Lake Tahoe, Nevada

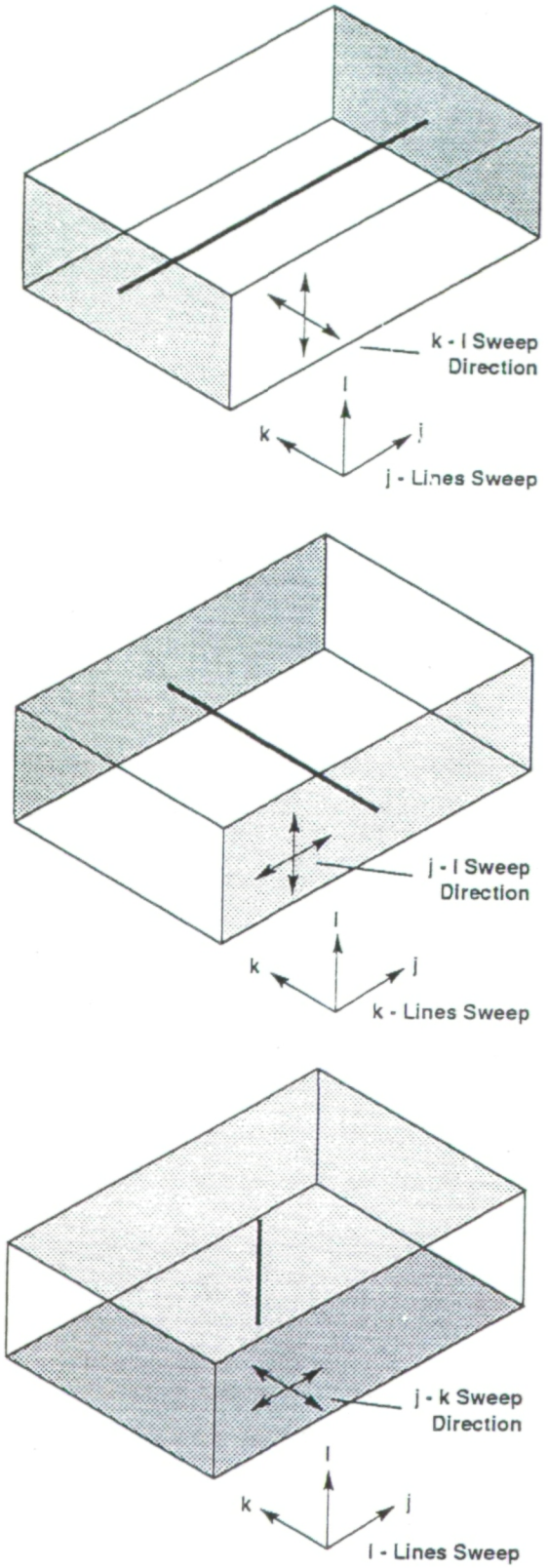

Fig. 1. Gauss-Seidel sweep directions.

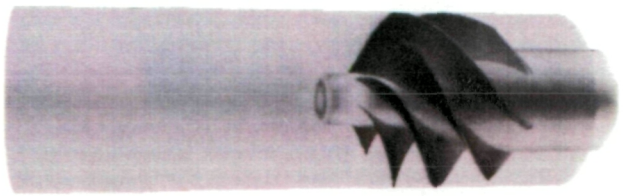

Fig. 2. Rocketdyne turbopump inducer configuration.

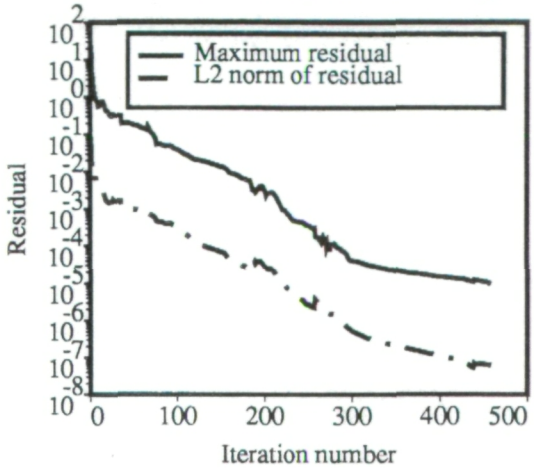

Fig. 3. Convergence history for inducer calculations.

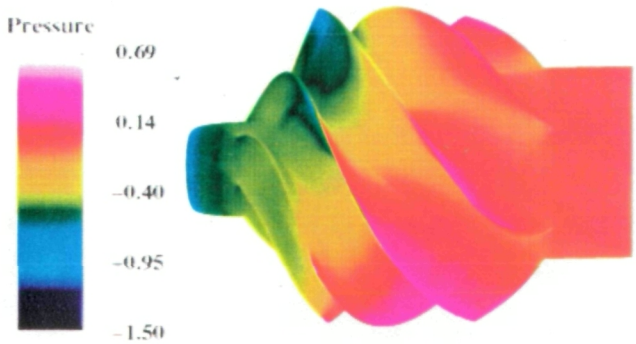

Fig. 4. Surface pressure of the pump inducer.

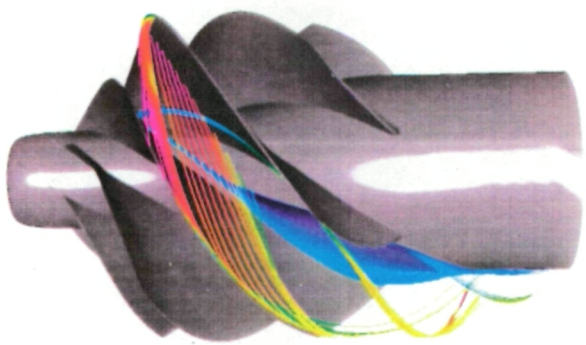

Fig. 5. Particle traces colored by relative total velocity magnitude.

ORIGINAL PAGE
COLOR PHOTOGRAPH

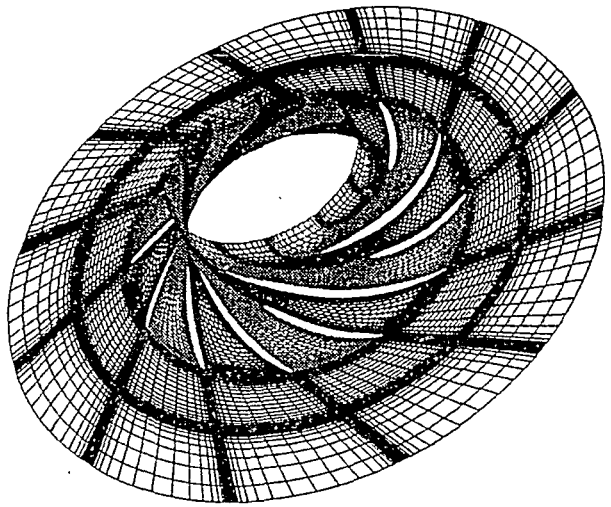

Fig. 6. Advanced pump impeller computational grid on the hub surface.

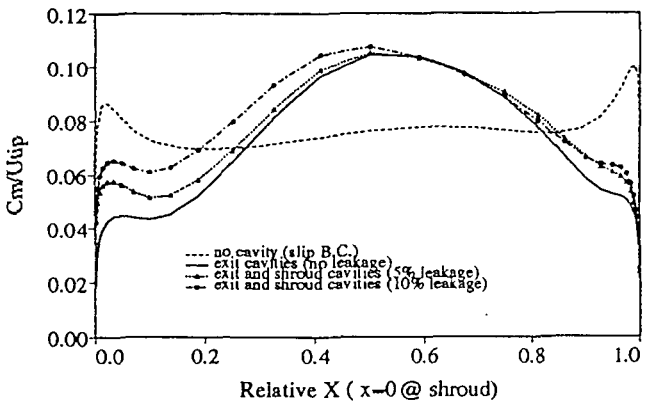

Fig. 7-a. Effect of the vaneless space on the impeller exit velocity.

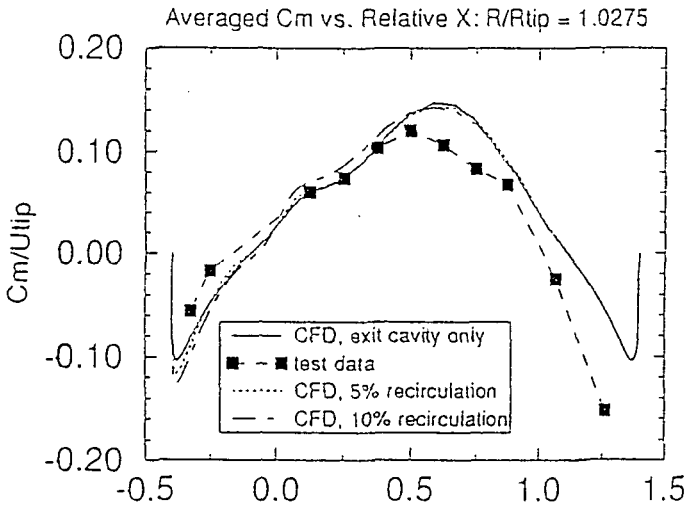

Fig. 7-b. Comparison of circulferentially averaged meridional velocity at the impeller exit.

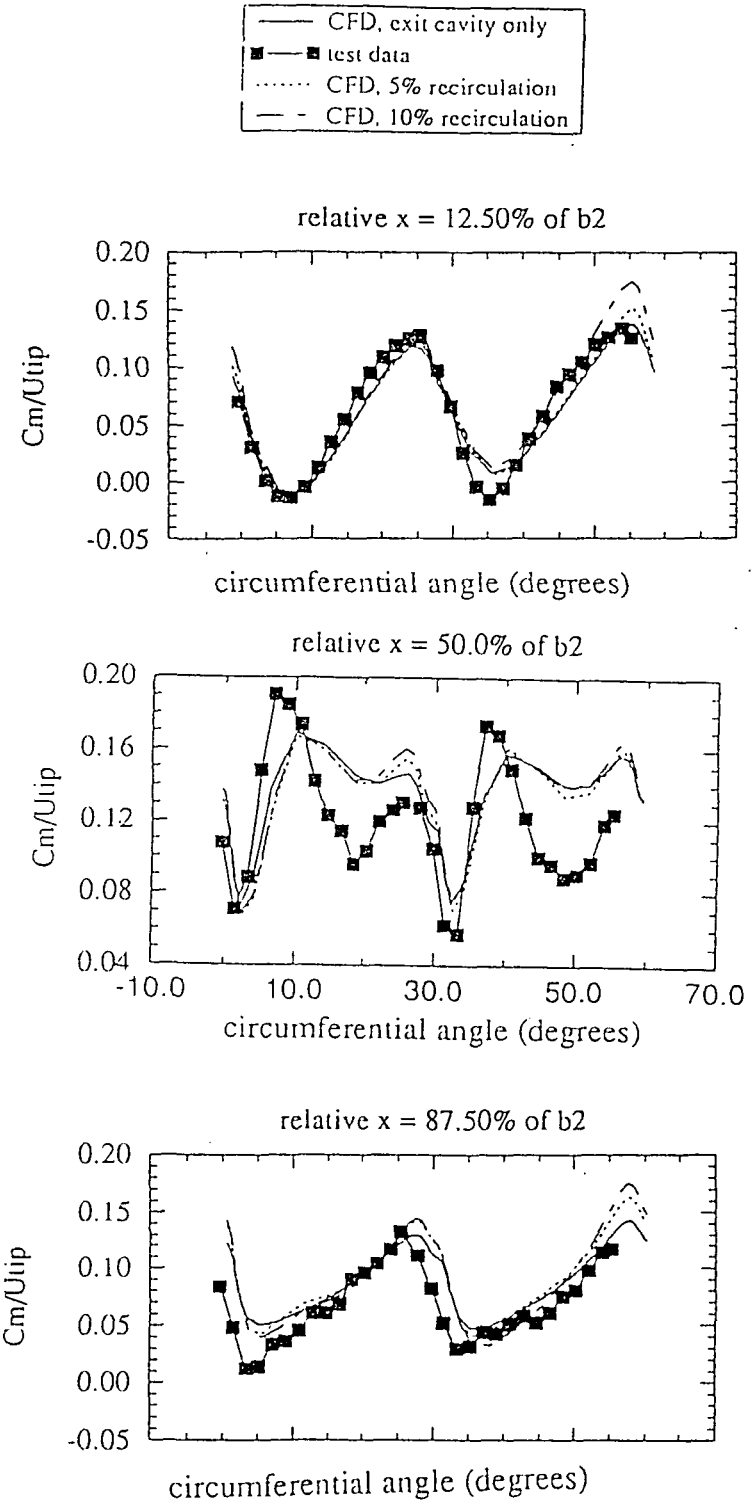

Fig. 8. Comparison of blade-to-blade meridional velocity at the impeller exit.

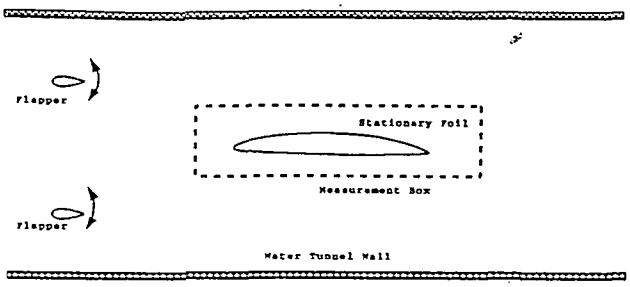

Fig. 9. Schematic of MIT Flapping Foil experiment (FFX).

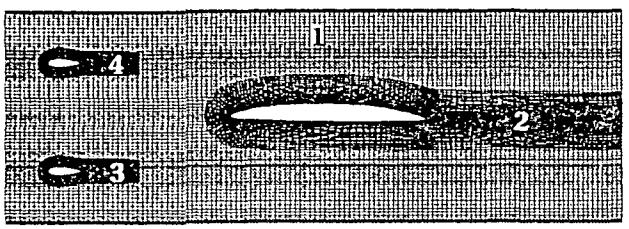

Fig. 10. Chimera overlapped grid topology for the FFX.

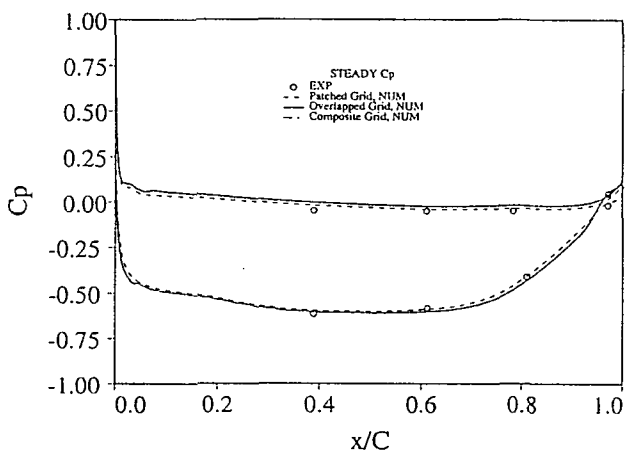

Fig. 11. Steady-state Cp distribution on the stationary foil

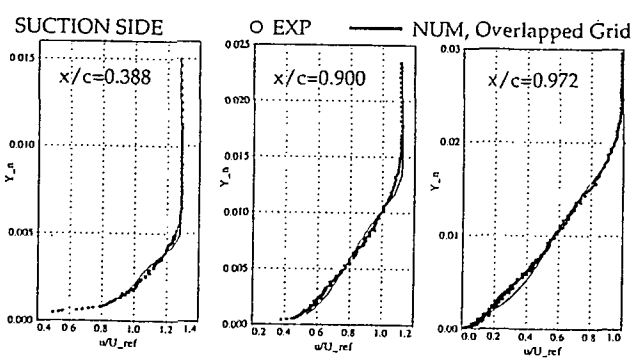

Fig. 12. Velocity profiles on upper surface of the stationary foil at streamwise stations of x/c=0.388, x/c=0.900, and x/c=0.972.

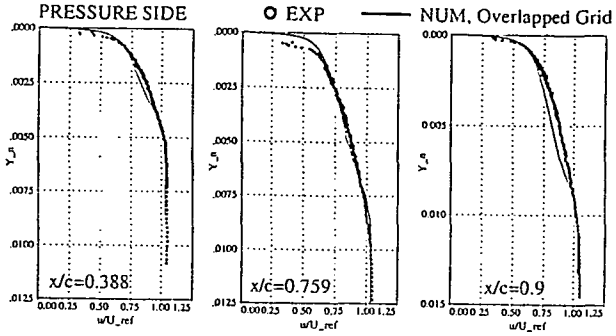

Fig. 13. Velocity profiles on lower surface of the stationary foil at streamwise stations of x/c=0.388, x/c=0.759, and x/c=0.900.

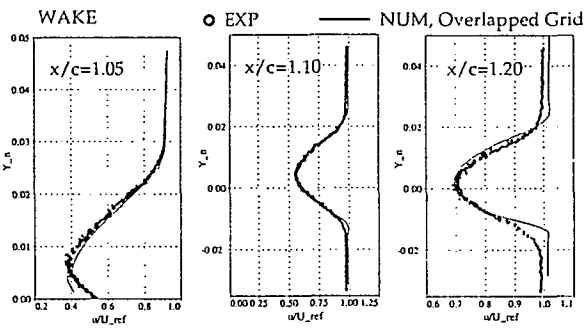

Fig. 14. Velocity profiles at the wake of the stationary foil at streamwise stations of x/c=1.05, x/c=1.10, and x/c=1.20.

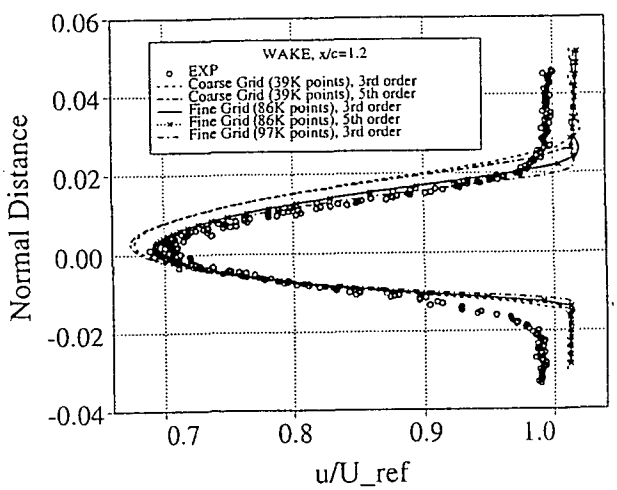

Fig. 15. Velocity profiles at the wake of the stationary foil at streamwise station of $x/c = 1.20$.

APPENDIX B

ASME Fluids Engineering Summer Meeting
Lake Tahoe, Nevada, June 19-23, 1994

TIME-ACCURATE INCOMPRESSIBLE NAVIER-STOKES COMPUTATIONS WITH OVERLAPPED MOVING GRIDS

Cetin Kiris
MCAT Institute, Mountain View, CA

Stuart Rogers, Dochan Kwak
NASA-Ames Research Center, Moffett Field, CA

and

Yu-Tai Lee
David Taylor Model Basin, Bethesda, MD

Abstract

A flapping foil experiment conducted at Massachusetts Institute of Technology was used as a validation case to evaluate the current incompressible Navier-Stokes approach with overlapped grid schemes. Steady-state calculations were carried out for overlapped and patched grids in which effects of the grid density and of the order of differencing were investigated. Numerical results showed good agreement with the experimental data. The resulting third-order upwind differencing and Baldwin-Barth one equation turbulence model were applied to unsteady flapping foil calculations. Two upstream NACA 0025 foils perform high-frequency synchronized motion and generate unsteady flow conditions for a downstream larger stationary foil. Fairly good agreement was obtained between unsteady experimental data and numerical results from two different moving boundary procedures.

Introduction

The next generation of transport vehicles with advanced component systems (e.g. high-lift configurations in the advanced subsonic systems, marine propulsion systems, advanced liquid rocket engine fuel system, etc.) in the near future are likely to require more efficient and simpler designs with lower manufacturing costs. Therefore, developing fast and reliable time-accurate incompressible flow simulation capabilities is an important task. For example, in order to understand the source of the noise generated by a high-lift wing-flap system, one needs to accurately resolve the unsteady air flow around these configurations. Another example of an unsteady incompressible flowfield is rotor-stator interaction in turbomachinary applications. A flange-to-flange rocket engine fuel-pump simulation includes an interaction between the rotating and non-rotating components, such as between flow straighteners, inducer-impeller, volute and diffusers. The unsteady incompressible flow simulations capability can also be beneficial to artificial heart device developers. A Ventricular Assist Device (VAD) developed by NASA Johnson Space Center and Baylor College of Medicine has flow straightener, inducer-impeller, and diffuser interaction which is similar to rotor-stator interaction described above for the fuel pump.[1] The technology developed for aerospace applications can be utilized for the benefit of the human health. Accurate and detailed knowledge of the flowfield obtained by unsteady flow calculations can be greatly beneficial for designers to reduce the cost and to improve the reliability of the advanced systems. In addition to geometric complexities, the challenges in these numerical simulations include turbulent boundary layer separation, wakes, transition, tip vortex resolution, three-dimensional effects, Reynolds number effects, the time-dependency and moving boundaries. As an example of complex physics in these examples, preliminary experimental efforts indicated that small amplitude oscillations of vibrating ribbons, flaps or fences delayed the separation of turbulent boundary layers and increased maximum lift generated by these airfoils.[2] A validated time-accurate incompressible Navier-Stokes (INS) solution procedure can be used to investigate the possible ways to control separation whenever the mean flow is unstable. In order to increase the role of Computational Fluid Dynamics (CFD) in the design process, the time-accurate algorithm needs to be evaluated and validated so that designers have the confidence to use it.

The current algorithm[3-4] for the incompressible Navier-Stokes equations is based on pseudocompressibility method which was introduced by Chorin.[5] The incompressible flow solvers developed at NASA Ames Research Center (the INS2D and INS3D family of codes) have been applied successfully to aerodynamic, turbomachinary, and artificial heart flow simulations: steady flow over high-lift aerodynamic configurations has been efficiently and accurately simulated;[6-8] the component analysis of the liquid rocket engine-pump flows validated the current approach in a steadily rotating frame of references;[9] wingtip vortex flowfield was studied using the present approach in steady-state;[10] A time-accurate artificial heart flow simulation with moving boundaries and some validation cases related to blood flow have been computed.[11] The objective of the current work is to validate the time-accurate formulation of the code for the flows with moving boundaries. An ideal validation case for this purpose has

been supplied by the Office of Naval Research (ONR) and Massachusetts Institute of Technology (MIT) Unsteady Flow Workshop held on March 29-30, 1993. ONR/MIT designed a flapping foil experiment (FFX) as a two-dimensional representation of the interaction between the propeller-blade and wake flows.[12] One purpose of the experiment is to provide detailed experimental data to be used to evaluate computational methods for marine propulsors. At the ONR/MIT workshop, the computed results obtained by various group of researchers were compared with experimental measurements. The flappers in the FFX generate high frequency periodic wake fluctuations which impose an unsteady loading on the stationary foil. In addition to the complexity of the flow physics, the numerical simulation of the FFX requires a proper domain decomposition and moving boundary procedures. This makes the FFX an attractive validation study for the current time-accurate formulation.

In the following section, the algorithm for the solution of incompressible Navier-Stokes equations is summarized. Next, the MIT FFX and the computational models for the FFX are described. Computed results from steady and time-accurate calculations using two different moving boundary procedures are then presented.

Algorithm

The present computations are performed utilizing the INS2D-UP[3] computer code which solves the incompressible Navier-Stokes equations for both steady-state and unsteady flows. The algorithm is based on the pseudocompressibility method as developed by Chorin.[5] The pseudocompressibility algorithm introduces a time-derivative of the pressure term into the continuity equation; the elliptic-parabolic type partial differential equations are transformed into the hyperbolic-parabolic type. The original version of the INS3D code[13-14] with pseudocompressibility approach utilized the Beam-Warming[15] approximate factorization algorithm and central differencing of the convective terms. Since the convective terms of the resulting equations are hyperbolic, upwind differencing can be applied to these terms. The current versions of the INS2D and INS3D codes use flux-difference splitting based on the method of Roe.[16] Chakravarthy[17] outlines a class of high-accuracy flux-differencing schemes for the compressible flow equations. Following the third-order upwind differencing, a fifth-order-accurate, upwind-biased stencil was derived by Rai.[18] The third and fifth-order upwind differencing used here is an implementation of these schemes for the incompressible Navier-Stokes equations. The upwind differencing leads to a more diagonal dominant system than does central differencing and does not require a user-specified artificial dissipation. The viscous flux derivatives are computed by using central differencing. In the steady-state formulation, the time derivatives are differenced using the Euler backward formula. The equations are solved iteratively in pseudo-time until the solution converges to a steady state. In the time-accurate formulation, the time derivatives in the momentum equations are differenced using a second-order, three-point, backward-difference formula.

$$\left(\frac{\partial U}{\partial \xi}+\frac{\partial V}{\partial \eta}\right)^{n+1}=0$$

$$\frac{3q^{n+1}-4q^{n}+q^{n-1}}{2\Delta t}=-r^{n+1}$$

where U, and V are contravariant velocity components, and where q and r denote the dependent variable vector and the right hand side vector for the momentum equations, respectively. After the discretization in time, the pseudocompressibilty term and pseudo-time level (m) are introduced to equations.

$$\frac{1}{\Delta\tau}(p^{n+1,m+1}-p^{n+1,m})=-\beta\nabla\cdot q^{n+1,m+1}$$

$$\frac{1.5}{\Delta t}(q^{n+1,m+1}-q^{n+1,m})=-r^{n+1,m+1}-\frac{3q^{n+1,m}-4q^{n}+q^{n-1}}{2\Delta t} \quad (1)$$

Here Δt, $\Delta\tau$, n, m, and β denote physical time step, pseudo-time step, physical time level, subiteration time level, and pseudocompressibility coefficient, respectively. The equations are iterated to convergence in pseudo-time for each physical time step until the divergence of the velocity field has been reduced below a specified tolerance value.

The matrix equation is solved iteratively by using a nonfactored Gauss-Seidel type line-relaxation scheme,[19] which maintains stability and allows a large pseudo-time step to be taken. Details of the numerical method can be found in Refs. 3-4. The present calculations use the one-equation turbulence model developed by Baldwin and Barth.[20] In this model, the transport equation for the turbulent Reynolds number is derived from a simplified form of the standard $k-\epsilon$ model equations. The model is relatively easy to implement because there is no need to define an algebraic length scale. The transport equation is solved by using the same Gauss-Seidel type line-relaxation scheme as the mean-flow equations.

MIT Flapping Foil Experiment and Computational Models

The purpose of the MIT FFX is to provide detailed unsteady measurements for CFD code validations. A schematic of the experimental set-up is given in figure 1. The stationary foil represents a propeller blade embedded in a wake flow generated by upstream pitching foils. The stationary foil has an 18-inch chord and a 1.18 degree angle-of-attack. The upstream flapping foils are NACA 0025 foils of 3-inch chord. The

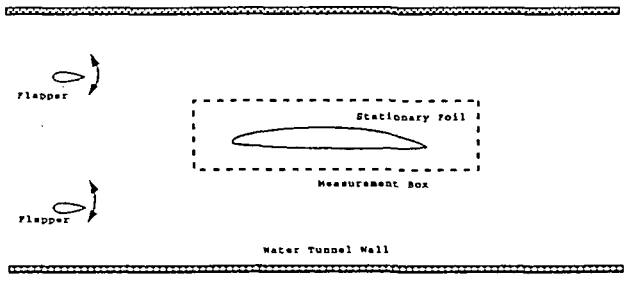

Figure 1. Schematic of MIT Flapping Foil experiment (FFX).

flappers perform synchronized sinusoidal motions of 6-degree amplitude at a reduced frequency of 3.62. Previous computations of the FFX include the following: a simplified configuration for the FFX was numerically simulated using a potential flow formulation;[22] a patched, time-varying, multi-block grid system was employed with a pseudocompressibility formulation by researchers at Mississippi State University[23] to simulate the FFX configuration; a chimera overlaid-grid scheme with a pressure-based method was used in the FFX simulation by Peterson and Stern.[24] In the present study, various grid topologies for the FFX configuration are studied, and the computed results obtained from a time-accurate pseudocompressibility formulation are compared with the experimental data.[12]

The flappers in the FFX generate periodic wake fluctuations which impose an unsteady condition on the stationary foil. Velocity and pressure measurements at a Reynolds number (based on the stationary foil chord and the inflow mean velocity) of 3.78×10^6 were taken on and around the stationary foil inside the measurement box, which is shown by the dashed line in figure 1. The box measurements were intended to provide the upstream, downstream, and outer boundary conditions for numerical calculations of the stationary foil alone. Since the purpose of the current numerical study is to investigate the moving boundary capability of the present unsteady incompressible Navier-Stokes solution procedure, the current computational model includes the entire domain shown in figure 1. The experimental conditions at the inlet and at the exit of

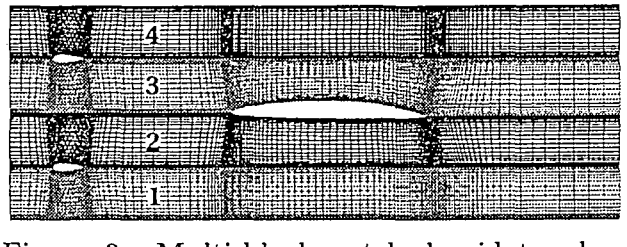

Figure 2. Multi-block patched grid topology for the FFX.

the water tunnel are specified numerically. In order to simulate the entire configuration, domain decomposition methods are utilized. Two commonly used domain decomposition methods for structured grids are multi-block patched[18] and chimera overlapped[21] grid schemes.

Figure 2 shows a multi-block patched grid topology applied to the FFX geometry, which contains four H-type grids. The patched grids are pointwise continuous at the zonal boundaries, and the interfaces have two points of overlap. Each grid has the dimension of 319x63, resulting in a total number of 80388 grid points. Every other grid lines were plotted in all grid related figures in this text. The patched grids were generated by GRIDGEN[25] with the elliptic grid generator option. Grid 1 occupies the region between the lower tunnel wall and the lower flapper surface; grid 2 extends between the lower flapper upper surface and the stationary foil pressure side; grid 3 is located between the stationary foil suction side and the upper flapper bottom surface; and grid 4 extends between the upper flapper top surface and the upper tunnel wall. The advantage of having this type of multi-block patched grid scheme is that the grids remain pointwise continuous as the bodies move, and thus there is no interpolation error at the interface boundaries. However, the grid has to be re-generated at each physical time step because of the flappers' motion. For the FFX, the interface boundaries between the zones move up or down with the flappers' rotation, and each zone experiences contraction and expansion during the cyclic motion.

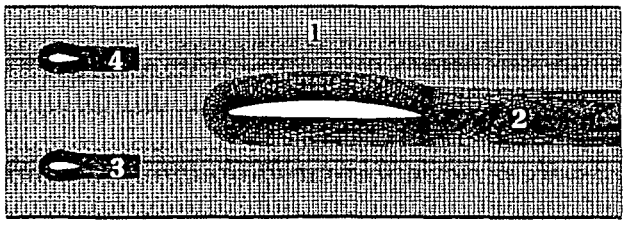

Figure 3-a. Chimera overlapped grid topology for the FFX.

An alternative to the multi-block patched grid scheme is the chimera overlapped grid scheme. The overlapped grid topology for the FFX is shown in figure 3-a. An H-type grid with the dimension of 253x191 (grid 1) occupies the water tunnel without considering the foils. Three C-type grids are generated for the foils and are overlapped with the tunnel grid. Grid 2 is generated for the stationary foil with the grid dimension of 337x61. Grids 3 and 4 wrap around the flappers with the grid dimension of 215x40; they rotate with the flappers. The total number of grid points for this grid system is 86080. Grid 1 was generated algebraically, and the C-type grids were generated by the HYPGEN[26] hyperbolic grid generator. The advantage of the chimera overlapped grid scheme as a moving boundary procedure is the simplification of the grid generation procedure. For the FFX, the grids are generated once, then the flapper grids are rotated relative to the tunnel grid. However, additional numer-

ical boundary conditions and the data management for the time-dependent interpolation stencils are introduced. The overlapped grid regions in the near-field of the flapper and in the near-field of the stationary foil leading edge are plotted in figure 3-b. The individual grids receive information from each other by interpolating the dependent variables. The grids around the foils have outer boundaries which overlap the interior region of the tunnel grid. The tunnel grid has an interior boundary surrounding a hole. A hole point is a mesh point which is removed from the solution procedure. The immediate neighbor points of the hole points are called fringe points and are updated from the interpolation procedure. For all computations presented in this paper, two-layer of fringe points are used

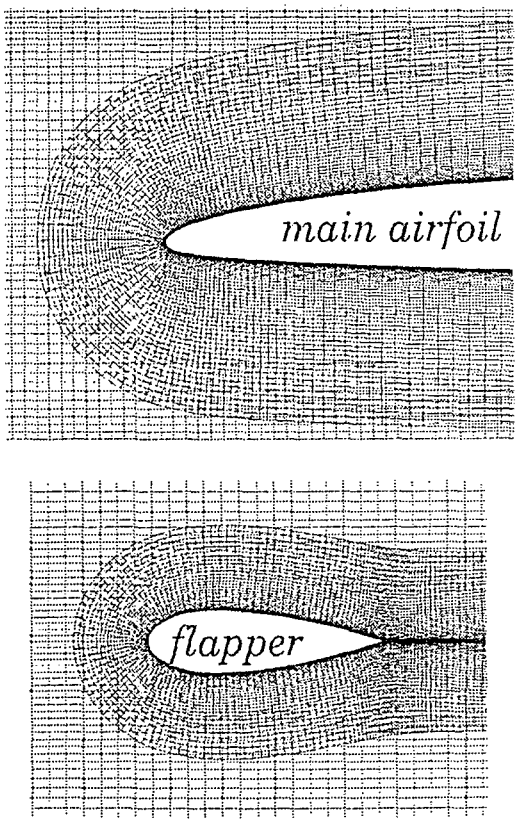

Figure 3-b. Overlapped grid regions in the near-field of the stationary foil and the flapper

for interior and outer boundaries. The PEGSUS[21] software is used to generate all interpolation information for each discrete position of the flapper grids. This grid topology is referred as "the overlapped grid" in the later text. For the overlapped grid topology of the FFX, the interpolation data between the flapper grid and the tunnel grid is time-dependent while the interpolation data between the stationary foil grid and the tunnel grid remains constant in time. The major difference between the patched and the overlapped grid approaches is the amount of effort required to generate the time-varying grids. Generating time-varying patched grid system for the FFX using the elliptic grid generator required an order of magnitude more work than generating the overlapped grid system and the interpolation data base. The overlapped grid system provides the flexibility of choosing grid topologies since the grids do not have constraints at boundaries. Therefore, the C-type hyperbolic grids can be easily used around the foils in which very fine grid resolution is required near the boundary layer. The patched grid system designed for the FFX required to use the H-type grid with the constraints at the boundaries. The elliptic grid generator were used for these H-grids. Obtaining the desired grid density near the boundary layer was the most time-consuming part in this procedure which had to be repeated at every boundary movement.

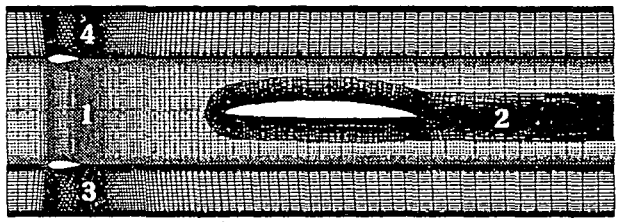

Figure 4. Composite grid topology for the FFX.

The last grid topology studied in this paper for the FFX is illustrated in figure 4. Both patched and overlapped grid schemes are employed in this grid system, referred as "the composite grid" in the later text. Three H-grids (grids 1, 3, and 4) are patched around the flappers by using the GRIDGEN elliptic grid generator. A C-grid around the stationary foil (grid 2) was generated by using the HYPGEN hyperbolic grid generator. In fact, grid 2 for the overlapped grid system and grid 2 for the composite grid system are identical. A hole is cut in grid 1 to accommodate the stationary foil. Grids 1 and 2 communicate with each other through the chimera interpolation procedure. The interpolation data between the stationary foil grid and the tunnel grid is not constant in time because the tunnel grid moves in time. Total number of grid points for this composite grid system is 77932, and the dimensions of the grids are 255x99, 337x61, 255x63, and 255x63, respectively.

Computed Results

In this section, the steady flow calculations with three different grid topologies are presented. The effects of grid density, and of the order of the differencing of the convective terms are investigated. Then the resulting procedure is applied to unsteady flow calculations.

Steady Flow Results

Since experimentally measured data was available for steady flow with stationary flappers with zero

degree angle of attack, steady-state calculations were carried out to validate the current approach before starting the more time consuming time-dependent calculations. The pseudocompressibility coefficient (β) was taken as 10 for all grid topologies in this section. Figure 5 compares the measured and calculated static pressure coefficient (Cp) on the stationary foil surface. The symbols represent the experimental measurements. The dashed line represents the patched grid results, the solid line represents the overlapped grid results, and the chaindotted line represents the composite grid results. All results show very good agreement with the measured data. The composite grid system Cp results are nearly identical to the overlapped grid results.

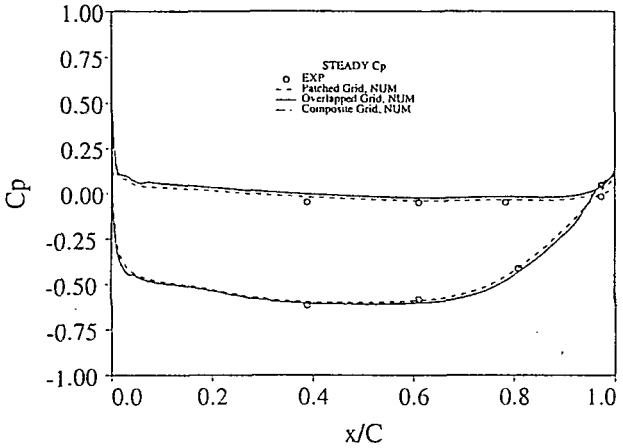

Figure 5. Steady-state Cp distribution on the stationary foil

Total velocity magnitude contours from the overlapped grid calculations are shown in figure 6. The wakes of the stationary foil and of the flappers are clearly seen. The contours from both grids in the overlapped regions match each other quite well. This ensures that the converged solution for the FFX steady-state case were obtained. The convergence history for this case is shown in figure 7. Converged solutions were obtained after 250 iterations which corresponds to approximately six minutes of CPU time on a Cray C90. Very similar convergence behavior was observed for all grid topologies. Even though the results did not change significantly after 250 iterations, 600 iterations were performed in order to show the behavior of the

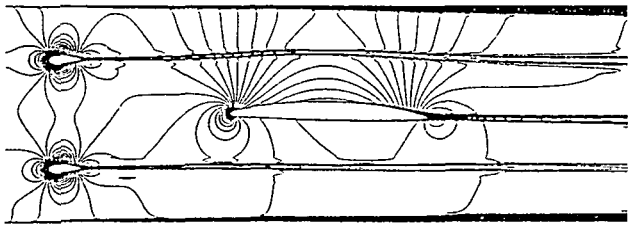

Figure 6. Steady-state total velocity magnitude contours.

convergence. The solid line in figure 7 shows the history of the maximum residual of the mean-flow equations. The dashed line shows the history of the maximum of the divergence of velocity, and the chaindotted line shows the history of the RMS of the Baldwin-Barth one-equation turbulence model. Figure 7 indicates that all three of these measures of convergence behave in a similar fashion.

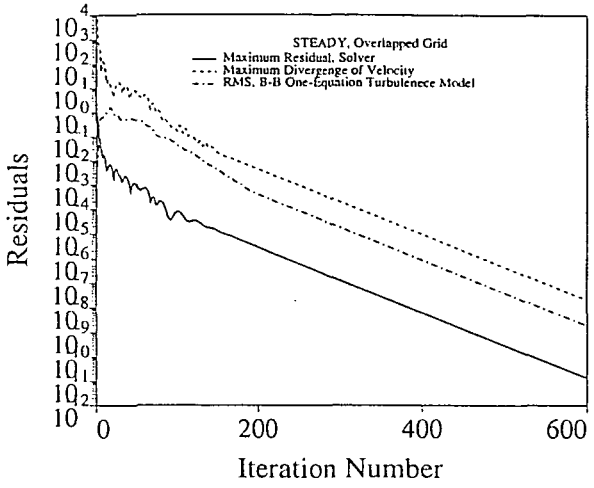

Figure 7. Convergence history for the FFX (overlapped grid topology).

The velocity profiles from the suction surface boundary layer of the stationary foil at the streamwise station of $x/c = 0.612$ are plotted in figure 8 for the three different grid topologies. These profiles plot the magnitude of the component of velocity that is tangential to the local stationary foil surface. This figure shows the effects of grid resolution near the stationary foil wall. The dashed and chaindashed lines represent the results from the patched grid system, in which each zone has an H-type grid generated by an elliptic grid generator. The elliptic grid generator does not provide exact control of the grid spacing at solid wall boundaries. Even though spacing on the order of 10^{-5} were specified as input to the elliptic grid generator, the resulting wall spacing was typically on the order of 10^{-3}. Therefore, the grid resolution near the stationary foil wall is quite poor for H-grids in this calculation. The velocity profile shown with the dashed line in figure 8 does not compare well with the experimental data. In order to improve the grid resolution near the wall region, the elliptic grid generator is being forced not to move the near wall points away from the wall. This result is shown with the chaindashed line. Although the velocity profile shown with the chaindashed line is improved compared to the one with the dashed line, it still does not compare well with the experimental data. The overlapped grid computations for the three levels of the grid density were carried out. The total number of grid points for the coarse overlapped grid system was 38607, and the dimensions of the grids were 127x96,

337x35, 215x34, and 215x34, respectively. The dimensions of the base overlapped grid system, which had total 86080 points, were given in the previous section.

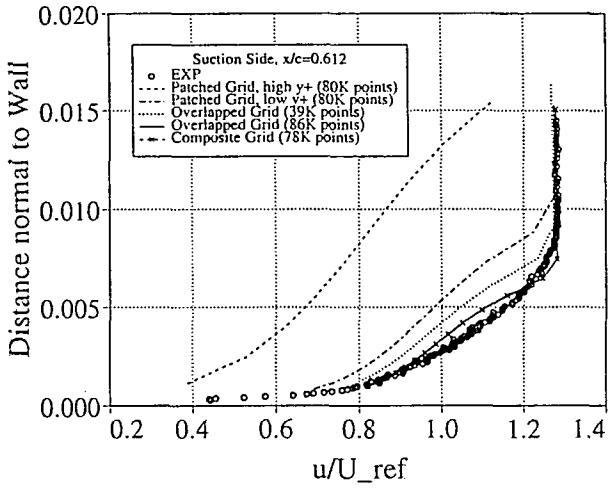

Figure 8. Velocity profiles on upper surface of the stationary foil at streamwise station of x/c=0.612.

The total number of grid points for the finest overlapped grid system was 97480, and the dimensions of the grids were 253x191, 337x91, 215x43, and 215x43, respectively. The dotted line in figure 8 represent overlapped grid results from the coarse grid. The grid spacing near the wall for the coarse grid is $2.5\text{x}10^{-4}$. The dotted line shows better agreement with the experimental data than patched grid results. The solid line represent the result obtained by using the base overlapped grid system and the dashed line with the x-mark symbols represent the result obtained by using the composite grid topology. The grid spacing near the stationary foil wall for these fine grids is $5.0\text{x}10^{-5}$. Both velocity profiles are virtually identical and compare fairly well with the measured data. These calculations use C-type hyperbolic grid for the stationary foil and clearly show the convenience of that approach over the H-type elliptic grid for airfoil type of configurations. The amount of work in generating H-type elliptic grid was increased when better grid resolution was required in the boundary layer region. Because of the easiness in the grid generation procedure, it was decided to use C-type hyperbolic grid around the stationary foil. Therefore, further computations in this text were focused on the overlapped grid topology and the composite grid topology. It should be pointed out that the composite grid topology still has patched H-grids around the flappers.

Figures 9 through 11 show the velocity profiles at several streamwise locations on the surfaces and at the wake of stationary foil. Symbols represent the experimental measurements and the solid lines represent numerical results obtained by using the overlapped grid topology. The velocity profiles from the composite grid topology are not included here because they are virtually identical with overlapped grid results (see figure 8). Figures 9 through 11 indicate that the computed results compare very well with the measured data at the boundary layer and the wake of the stationary foil. The biggest discrepancy between the computed results and the measured data is seen in the wake of the foil (x/c=1.2). The velocity at the edge of the wake is

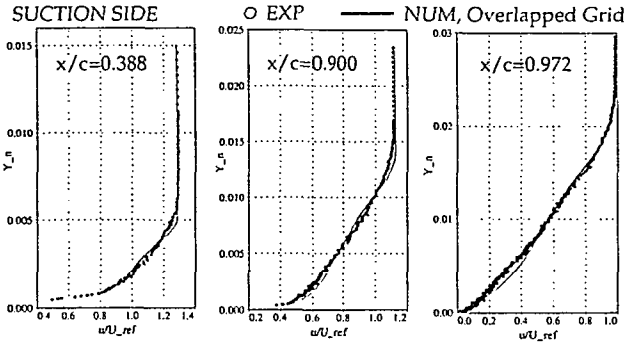

Figure 9. Velocity profiles on upper surface of the stationary foil at streamwise stations of x/c=0.388, x/c=0.900, and x/c=0.972.

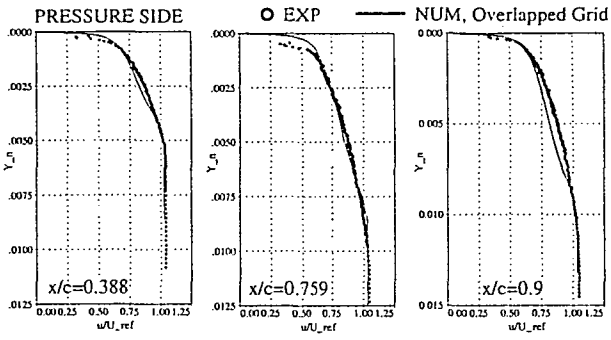

Figure 10. Velocity profiles on lower surface of the stationary foil at streamwise stations of x/c=0.388, x/c=0.759, and x/c=0.900.

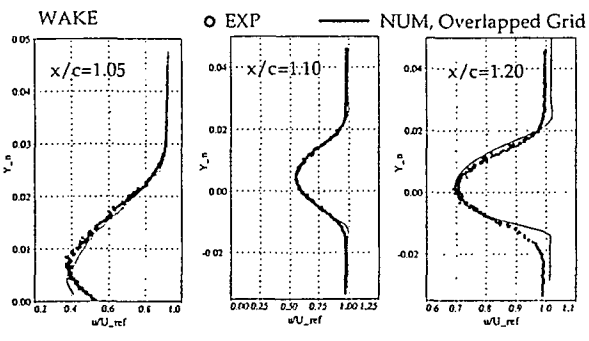

Figure 11. Velocity profiles at the wake of the stationary foil at streamwise stations of x/c=1.05, x/c=1.10, and x/c=1.20.

overpredicted with less then a couple of percent error range. In order to make sure the steady flow results are grid independent, some additional computations

were carried out. The order of accuracy for convective terms in coarse grid calculations was increased from third-order to fifth-order flux difference splitting. The third-order coarse grid result is shown with the dashed line and the fifth-order coarse grid result is shown with the chaindashed line in figure 12. The solid line and the dotted line with x-marks represent the fine grid third-order and fifth-order results, respectively. The

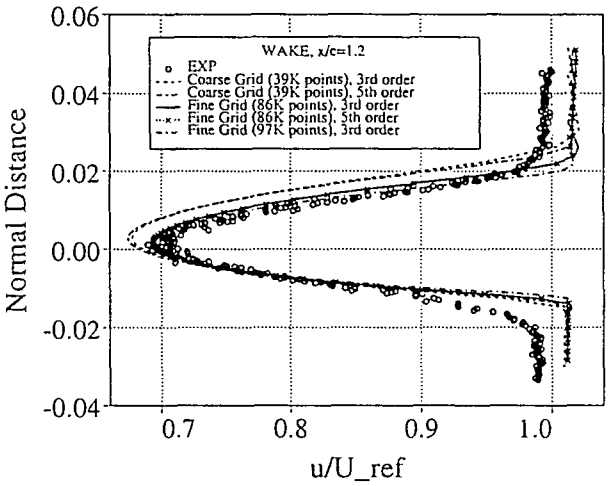

Figure 12. Velocity profiles at the wake of the stationary foil at streamwise station of x/c = 1.20.

wake from the fine grid computations clearly show better agreement than the coarse grid does with the measured data. The overshoot which occurs at the edge of the wake in the third-order results does not occur in the fifth-order results. In the finest grid computations, the base grid for the stationary foil was refined by increasing the number of grid points in the normal direction from 61 to 91. The velocity profile from the resulting finer grid (total 97K points) with the third-order differencing is plotted with the chaindotted line. This fine grid result is very similar to the base grid (86K grid point) result, indicating that this is close to grid independent solution and that 86K point grid will provide adequate resolution for the unsteady calculations. In fact, the difference between the 86K and the 97K grid results is less than the oscillations in the measured data. Notethat there is a rather large differencing between the measured and computed wake edge velocities. Since this edge velocity is shown to be grid independent, it is thought that the experimental data used an erroneous value for the reference velocity for this data. In addition, all computed results have the same velocity magnitude at the edge of the wake and fine grid results are self consistent. Because of these reasons, the result shown with solid line in figure 12 is considered to be a reasonably grid independent solution. At this point, it is believed that the computational procedure is ready for the unsteady flapping foil calculations.

Unsteady Flow Results

The converged steady solutions were used as the initial conditions for the unsteady calculations. The motion of flappers was specified as a pitching about the mid-chord point described by $\alpha = \alpha_m sin(wt)$, where t is time, α_m is six degree and the angular velocity is described by $w = 2kU_\infty/c$. Here U_∞ is the reference velocity specified as 20.62 $feet/sec$ and c is the stationary foil chord specified as 18 inches. The reduced frequency k is 3.62 based on $c/2$. In all unsteady calculations, one cycle of the flapping foil period consisted of 192 physical time steps, which corresponds to a discrete nondimensional time step of $4.53\text{x}10.^{-3}$ The time-step size was chosen to be small enough so that the moving mesh points in the overlapped grid system does not move through more than one cell in a neighboring grid during one time step. At each physical time-step, the maximum of non-dimensional divergence of velocity was dropped below 10^{-2} for all zones. This required between 15 to 40 subiterations during each time-step. Numerical tests indicated that reducing the divergence of velocity lower than this had no effect. The pseudo-time step ($\Delta\tau$) was taken the same value as physical time step (Δt). The pseudo-compressibility coefficient β was set to 10. With these conditions, one period of the flapping foil was obtained in 3.5 to 4 Cray C90 hours. The periodic solution was obtained for both grid topologies after six flapping cycles.

(a) with the overlapped grid topology

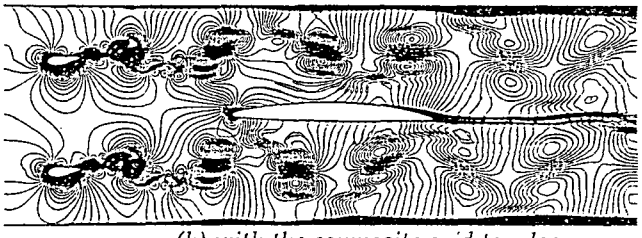

(b) with the composite grid topology

Figure 13. Unsteady velocity magnitude contours obtained by using two different grid topologies at $t/T = 0.25$.

Total velocity magnitude contours at a nondimensional time of $t/T = 0.25$ are shown in figure 13 for both the overlapped grid topology (top figure) and the composite grid topology (bottom figure). Here T denotes the period of the flappers' motion. This qualitative comparison shows that the results are very

similar. This unsteady wake is resolved slightly better in the composite grid topology than it is in the overlapped grid topology. Since the grid patch boundaries lay in the region where the oscillating wakes are located, the finer grid resolution in the patched grid boundary region results in the better resolution of the wakes. However, the difference between the two results is not so recognizable from the contours. The quantitative comparison between the two and the experimental data is presented in figures 14 through 16.

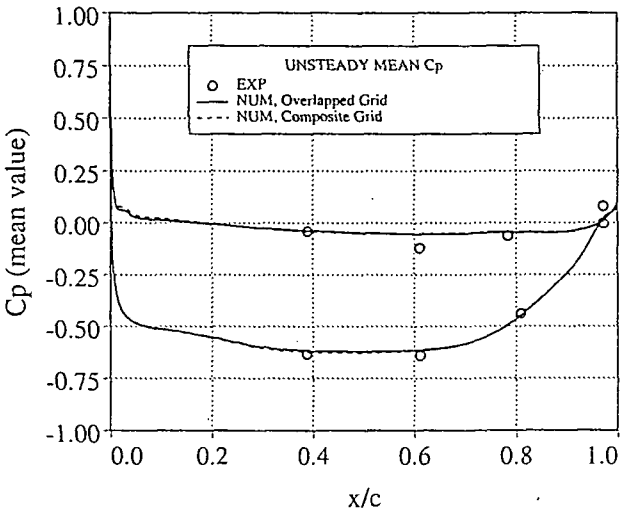

Figure 14. Unsteady mean Cp distribution on the stationary foil

The mean Cp distributions on the stationary foil surface from the unsteady calculations are plotted in figure 14. The symbols represent the experimental mean values. The solid lines represent the overlapped grid results, and the dashed lines represent the composite grid results. The computed mean Cp values compare very well with the experimental measurements, except there is a slight overprediction at the 60% of chord location on the pressure side of the foil. The mean Cp values from two different grid topologies show identical behavior. The time history of Cp values at several streamwise locations of the stationary foil are compared with experimental data in figure 15. The Cp values obtained from both grid topologies show a very similar time history. They both compare fairly well with the measured data. The biggest discrepancies are seen on the pressure side of the foil at streamwise location $x/c = 0.611$ where Cp is overpredicted and on the suction side of the foil at streamwise location $x/c = 0.972$ where Cp is underpredicted. This is consistent with the mean Cp distribution in Figure 14. The major difference between the two computed results is that overlapped grid topology predicts some higher frequency oscillations that the composite grid scheme does not. It should be noted that the grid movement and the number of overset grid boundary interpolations in the composite grid topology is considerably smaller compared to the overlapped grid topology. In the overlapped grid topology, as the flapper grids rotate they move through relatively coarse region in the tunnel grid. This mismatch of the grid resolution between overlapped grids can lead to interpolation errors and an inability of grid to resolve the flapper wakes. Considering that different hole points are being cut at each time step while locally refined flow feature moves in time (unsteady wakes from flappers), obtaining the same degree of accuracy between the two grids is not an easy task. In the composite grid system, the mesh points in the tunnel grid move with the flappers which maintains relatively fine grid resolution in the near wakes of the flappers. Improvements of the accuracy for the overset grids are currently being researched. Recently, a defect correction approach[27] has been introduced to enhance accuracy for overset grids. The FFX simulation with overlapped grid topology would be a good test case for the defect correction scheme in the future.

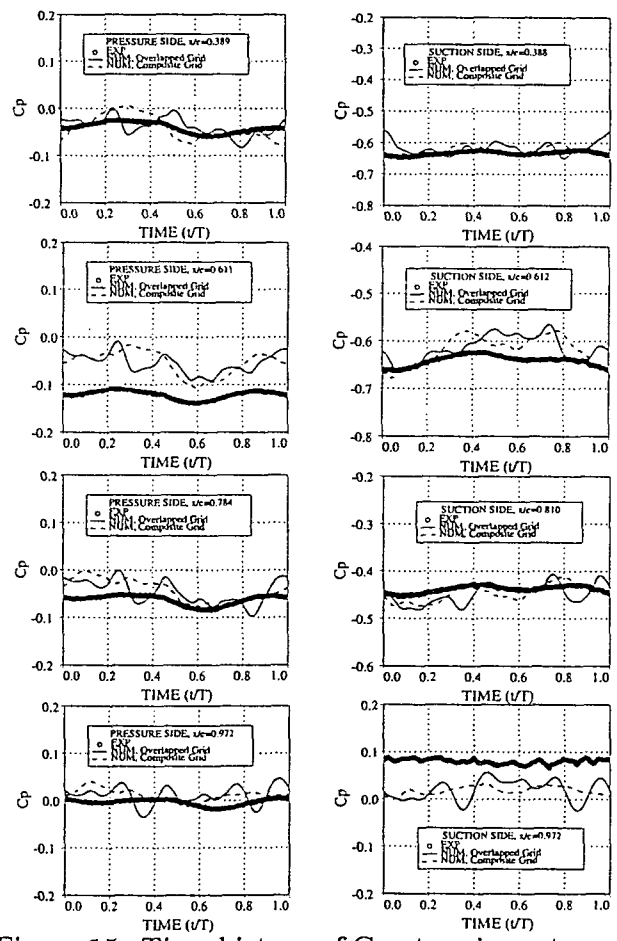

Figure 15. Time history of Cp at various streamwise locations of the stationary foil.

Figure 16 illustrates the effect of the improper use of the interpolation information when computing previous time level data for newly created fringe points. The time history of Cp on the suction side of the foil at streamwise location $x/c = 810$ is replotted for the composite grid topology. The symbols represent the

experimental measurements. The procedures for updating previous time level data at the fringe points are different between the two computed results shown by the solid line and by the dashed line. As shown in equation 1, information at time levels n and $n-1$ is neccesarry to advance to the $n+1$ time-level. When a hole point becomes a fringe point due to moving boundaries this fringe point does not have any information from the previous time levels. One way to obtain the previous-time level data is to interpolate the variables from the donor grid (as it is done for the current time-level information). The result obtained by this procedure is plotted by the dashed line in figure 16. This shows that very large amplitude errors are occuring in the computations. The source of these fluctuations can be found in the interpolating procedure. The previous time-level data for the new fringe points is obtained by using the interpolation data base at the current time level. However, the grid point locations from the previous time-level should have been used. Using the current time-level data base for these points results in incorrect interpolation coefficients and incorrect donor points. When this error was corrected, the computed Cp value shown by the solid line in figure 16 was obtained. When the previous time-level data is not available for the newly created boundary points, the time integration for these points is changed to first-order. The time-differencing in the next time step will be second-order backward differencing because the previous time-level information is established from the current time step.

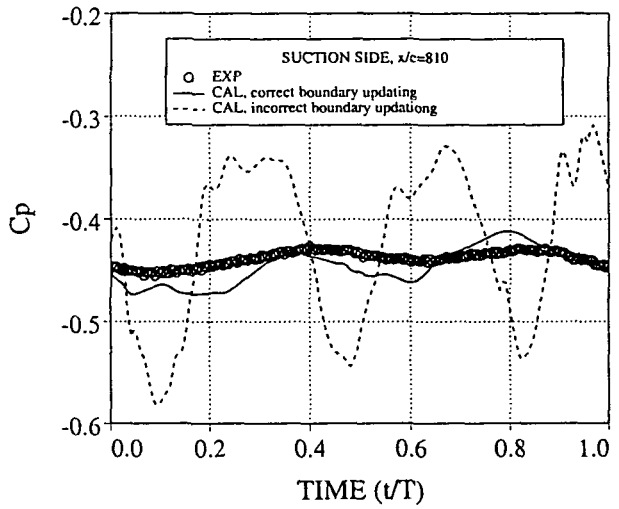

Figure 16. The effect of updating boundary points in the overlaid moving regions of the composite grid system.

Conclusions

An incompressible flow solver in steady and time-accurate formulations has been utilized for the MIT flapping foil experiment. A detailed study for the steady-state calculations was performed to investigate the effects of grid topology, grid resolution, and the order of accuracy. The one-equation Baldwin-Barth turbulence model was able to accurately compute the Cp and boundary layer velocity distribution on the stationary airfoil. A nearly grid independent solution was obtained for the steady FFX simulation by using third-order flux-difference splitting for the convective terms. Overall, the computed steady-state results showed good agreement with the experimentally measured Cp and boundary layer profiles on on the stationary foil.

Unsteady computations were performed using two different grid topologies. Good agreement with experimental mean pressure coefficient were obtained for both grid topologies. The time history of Cp on the stationary foil at several streamwise locations was presented for the two grid topologies. Initial attempts of the computations on both types of grid topologies resulted in high-frequency errors of large magnitude. The error was found to come from an improper use of the interpolation information when computing previous time level data for newly created fringe points. This was fixed by changing the time-integration for such points to first-order. When updating the boundary points in the overset grids is done properly, the computed results are in fairly good agreement with the experimental data. However, the overlapped grid calculations still tend to generate erroneous oscillations in time. The composite grid computations also show some of this type of error, but to a much smaller extent. Further investigation into the source of these errors is on going.

Acknowledgments

This work was partially supported by NASA Marshall Space Flight Center. The work of the first author was supported by NASA Ames Research Center through Cooperative Agreement NCC 2-500. Computer time was provided by the Numerical Aerodynamic Simulation (NAS) Facility and the Central Computing Facility at NASA Ames Research Center. The authors would like to thank Mr. Leon Chang of MCAT Institute for providing grid generation support.

References

[1] Aber, G. S., Akkerman, J.W., Bozeman, R. J., and Saucier, D. R., "Development of The NASA / Baylor VAD," NASA Technology 2003 Conference, 1993.

[2] Katz, Y., Nishri, B., and Wygnanski, I., "The Delay of Turbulent Boundary Layer Separation by Oscillatory Active Control," AIAA Paper No. 89-1027, 1989.

[3] Rogers, S. E., Kwak, D., "Upwind Differencing for the Time-Accurate Incompressible Navier-Stokes Equations," *AIAA Journal* , Vol. 28, No. 2, pp. 253-262, 1990.

[4] Rogers, S. E., Kwak, D. and Kiris, C., "Numerical Solution of the Incompressible Navier-Stokes Equations for Steady and Time-Dependent Problems," *AIAA Journal* , Vol. 29, No. 4, pp. 603-610, 1991.

[5] Chorin, A., J., "A Numerical Method for Solving Incompressible Viscous Flow Problems," *Journal of Computational Physics,* Vol. 2, pp. 12-26, 1967.

[6] Rogers, S. E., Wiltberger, N. L., and Kwak, D. "Efficient Simulation of Incompressible Viscous Flow Over Single and Multi-Element Airfoils," AIAA Paper No. 92-0405, 1992.

[7] Rogers, S. E., "Progress In High-Lift Aerodynamic Calculations," AIAA Paper No. 93-0194, 1993.

[8] Rogers, S. E., "A Comparison of Turbulence Models In Computing Multi-Element Airfoil Flows," AIAA Paper No. 94-0291, 1994.

[9] Kiris, C., Chang, L., Kwak, D., and Rogers, S. E., "Incompressible Navier-Stokes Computations of Rotating Flows," AIAA Paper No. 93-0678, 1993.

[10] Dacles-Mariani, J., Rogers, S. E., Kwak, D., Zilliac, G., and Chow, J., "A Computational Study of Wingtip Vortex Flowfield," AIAA Paper No. 93-3010, 1993.

[11] Kiris, C., Rogers, S. E., Kwak, D. and Chang, I. "Computation of Incompressible Viscous Flows through Artificial Heart Devices with Moving Boundaries," Fluid Dynamics in Biology, Proceedings of an AMS-IMS-SIAM Joint Research Conference, edited by A. Y. Cheer and C. P. van Dam, American Mathematical Society, Providence, R. I., 1991, pp. 237-247.

[12] Kerwin, J., Keenan, D., Maxel, C., Horwich, E., and Knapp, M., "MIT/ONR Flapping Foil Experiment," MIT/ONR FFX Workshop, David Taylor Model Basin, March 1993.

[13] Kwak, D., Chang, J. L C., Shanks, S. P., and Chakravarthy, S., "A Three-Dimensional Incompressible Navier-Stokes Flow Solver Using Primitive Variables," *AIAA Journal* , Vol. 24, No. 3, pp. 390-396, 1977.

[14] Chang, J., Kwak, D., Rogers, S. E., and Yang, R.-J., "Numerical Simulation Methods of Incompressible Flows and an Application to the Space Shuttle Main Engine," *International Journal of Numerical Methods in Fluids*, Vol 8, pp. 1241-1268, 1988.

[15] Beam, R. M., Warming, R. F., " An Implicit Factored Scheme for the Compressible Navier-Stokes Equations," *AIAA Journal* , Vol 16, pp. 393-401, 1978.

[16] Roe, P.L., "Approximate Riemann Solvers, Parameter Vectors, and Difference Schemes," *Journal of Computational Physics,* Vol. 43, pp. 357-372 1981

[17] Chakravarthy, S. R., Osher, S., "A New Class of High Accuracy TVD Schemes for Hyperbolic Conservation Laws," AIAA Paper No. 85-0363, 1985.

[18] Rai, M. M. "Unsteady Three-Dimensional Navier-Stokes Simulations of Turbine Rotor-Stator Interaction," AIAA Paper No. 87-2058, 1987.

[19] MacCormack, R., W., "Current Status of Numerical Solutions of the Navier-Stokes Equations," AIAA Paper No. 85-0032, 1985.

[20] Baldwin, B., S. and Barth, T., J., "A One-Equation Turbulence Transport Model for High Reynolds Number Wall-Bounded Flows," AIAA Paper No. 91-0610, 1991.

[21] Benek, J.A, Buning, P. G., and Steger, J. L., "A 3-D Chimera Grid Embedding Technique," AIAA Paper 85-1523, July 1985.

[22] Lee, Y. T., Feng, J., and Merkle, C. L., "Time-Dependent Inviscid Flow Analysis of Rotor-Stator Systems," Sixth Int. Conf. on Numerical Ship Hydrodynamics, August 2-5, 1993.

[23] Taylor, L. K., Busby, J. A., Jiang, M. Y., Arabashi, A., Sreenivas, K., and Whitfield, D. L., "Time Accurate Incompressible Navier-Stokes Simulation of the Flapping Foil Experiment," Sixth Int. Conf. on Numerical Ship Hydrodynamics, August 2-5, 1993.

[24] Paterson, E., Stern, F., "Computation of Unsteady Viscous Flow with Application to the MIT Flapping-Foil Experiment," Sixth Int. Conf. on Numerical Ship Hydrodynamics, August 2-5, 1993.

[25] Steinbrenner, J., Chawner, J. and Fouts, C., " The GRIDGEN 3D Multiple Block Grid Generation System," User's Manual, WRDC-TR-90-3022, Vils. I and II, Wright Patterson Air Force Base, 1990.

[26] Chan, W. M., Chiu, I. T. and Buning, P. G., "User's Manual for the HYPGEN Hyperbolic Grid Generator and the HGUI Graphical User Interface," NASA TM 108791, October, 1993.

[27] Rogers, S. E., and Pulliam T. H., "Accuracy Enhancements for Overset Grids Using a Defect Correction Approach," AIAA Paper No. 94-0521, 1994.